Modelling of deformations of high strength concrete at elevated temperatures

D. Gawin[1], F. Pesavento[2] and B. A. Schrefler[2]

(1) Department of Building Physics and Building Materials, Technical University of Łódź, Al. Politechniki 6, 93-590 Łódź, Poland

(2) Department of Structural and Transportation Engineering, University of Padua, via Marzolo 9, I-35131 Padua, Italy

ABSTRACT

A constitutive model for the analysis of deformations of concrete subject to transient temperature and pressures is proposed. In these severe conditions concrete structures experience spalling phenomenon, which is the violent or non-violent breaking off of layers or pieces of concrete from the surface of a structural element when it is exposed to high and rapidly rising temperatures. This process can lead to a loss of load-bearing capacity, trough a loss of section and a loss of protection to steel reinforcement. Many different form of spalling exist, but probably the most dangerous is explosive spalling, because it is sudden and capable to result in a general collapse of the structure.

The constitutive model includes thermo-chemical and mechanical damage for taking into account the deterioration of the material due to mechanical loads, high temperatures and chemical changes and it is introduced into a general coupled mathematical model of hygro-thermo-chemo-mechanical behaviour of concrete structures.

In this constitutive model the so called free thermal strains, which are the concrete strains during first heating, are decomposed in three main contributions: thermal dilatation strains (treated in a manner usual in thermo-mechanics), shrinkage strains (modelled by means of the effective stress principle) and thermo-chemical strains (which take into account for the thermo-chemical decomposition of the concrete and which are related to thermo-chemical damage). Thermo-mechanical strains occurring during first heating of concrete under load, known as LITS (Load Induced Thermal Strains), are also included in the framework of thermodynamics of porous media. The proposed model is applied to an illustrative example that demonstrates its capabilities.

RÉSUMÉ

Nous proposons un modèle pour l'étude des déformations du béton sous variations de température et pression. Dans ces conditions extrêmes, le béton subit l'écaillage qui est une rupture violente ou non de couches ou pièces de béton sur la surface d'éléments structurels soumis à haute température ou température augmentant rapidement. Ce fait peut produire une diminution de la capacité portante à travers une diminution de la section ou la perte de protection du maillage. Il y a différentes formes d'écaillage mais le plus dangereux est probablement l'écaillage explosif car il est sans préavis et entraîne l'écroulement de la structure.

Le modèle constitutif inclut l'endommagement thermochimique et mécanique pour prendre en compte la détérioration du matériau due aux charges mécaniques, aux hautes températures et aux chargements chimiques.

Tout ceci est introduit dans un modèle mathématique couplé pour la description du comportement hygro-thermochimique et mécanique des structures en béton. Dans ce modèle constitutif, les déformations thermiques libres, c'est à dire les déformations dans le béton pendant le premier échauffement sont décomposés en trois parties: déformations dues à la dilatation thermique (traitées selon la manière habituelle de la thermomécanique), déformations dues au séchage (modèles à l'aide des contraintes effectives) et déformations thermochimiques (qui prennent en compte la décomposition thermochimique du béton et qui sont liées à l'endommagement thermochimique). Les déformations thermomécaniques qui ont lieu pendant le premier échauffement du béton sous charge, généralement connues sous le nom de LITS (Load Induced Thermal Strain) sont aussi inclues dans le cadre de la thermodynamique des milieux poreux. Le modèle proposé est appliqué à un exemple pour démontrer ses capacités.

1. INTRODUCTION

With increasing use of high-strength concrete (HSC) for building and other structural applications (*e.g.* high-rise buildings, bridges and tunnels), behaviour of the material at high temperature became an important subject of many

researches during the last decade, *e.g.* [1-17]. HSC provides better structural performance, especially in terms of strength and durability, compared to traditional, normal-strength concrete (NSC). However, many studies, *e.g.* [4-6], showed that the fire performance of HSC differs from that of NSC which exhibits rather good behaviour in these conditions. The major problem with HSC structures exposed to high temperature is thermal spalling, which results in rapid loss of the surface layers of the concrete at temperature exceeding about 200-300°C. As a result, the core concrete is exposed to these temperatures, thereby increasing the rate of heat transmission to the core part of the element and in particular to the reinforcement, what may pose a risk for the integrity of concrete structure.

It is commonly believed that the main reasons of the thermal spalling are: build-up of high pore pressure close to the heated concrete surface as a result of rapid evaporation of moisture, and the release of the stored energy due to the thermal stresses resulting from high values of restrained strains caused by temperature gradients [4-9]. Nevertheless, relative importance of the two factors is not established yet and still needs further studies, both experimental and theoretical. The results of the research performed up to now show that the fire performance of HSC structures is influenced by several factors [1-17], like initial moisture content of the concrete, the rate of temperature increase (fire intensity), porosity (density) and permeability of the concrete, its compressive strength, type of aggregate, dimensions and shape of a structure, its lateral reinforcement and loading conditions. Recently, a statistical significance of the aforementioned factors and their mutual interactions were analysed by means of the ANOVA method (analysis of variance) applied to the results of some specially planned, systematic experimental studies, [13, 16].

Deformations of concrete subjected to high temperature and mechanical load, and in particular the phenomenon of so-called thermal transient creep resulting in load induced thermal strains (LITS), are of great importance for proper evaluation of the performance of concrete structures in those conditions. In this paper we analyse some results of thermo-physical, chemical and mechanical tests of HSC performed within the "HITECO" project [6], and formulate from them a model and some constitutive relations for concrete deformations at high temperature, including LITS. A strong coupling between processes of concrete deformation and its thermo-chemical deterioration, evident from these results, is taken into account in the proposed constitutive model for the description of the material deformations. This is introduced then in our mathematical model of hygro-thermo-chemo-mechanical behaviour of concrete at high temperature [9, 14, 15, 17], and applied for solution of some numerical examples.

2. MODELLING LFTS OF UNLOADED CONCRETE AT HIGH TEMPERATURE

An unloaded sample of plain concrete or cement stone, exposed for the first time to heating, exhibits considerable changes of its chemical composition, inner structure of porosity and changes of sample dimensions (irreversible in part). The latter ones are a result of several complicated physicochemical phenomena, often acting in opposite directions, like thermal expansion, material cracking, cement and aggregate dehydration and skeleton shrinkage.

A part of these strains is irreversible in nature and remains as residual strains even after cooling of the sample to the ambient temperature. The concrete strains during first heating, called load-free thermal strains (LFTS) are usually treated as superposition of thermal and shrinkage components, and are often considered as almost inseparable. A proposal of isolation of the shrinkage component from the experimentally determined LFTS is presented in [18], but its physical basis is not convincing, and furthermore it cannot be used directly in numerical modelling. For this purpose a clear definition of physical mechanisms and corresponding components of concrete strains with appropriate mathematical description are needed. A proposal of such a model, slightly different from that described in [3], is presented further in this section.

Our considerations will be illustrated by the analysis of results of the thermal dilatation tests of two types of high strength concrete, C-60 and C-90 (Fig. 1), the composition, inner structure and physical properties of which were described in [6], and are briefly summarised in Table 1.

2.1 Thermal dilatation strains

The analysed types of HSC, exposed to increasing temperature, expand as can be seen in Fig. 1. A reversible part of their deformation, corresponding to the decreasing-temperature-branch of the experimental curve ("exp. cooling"),
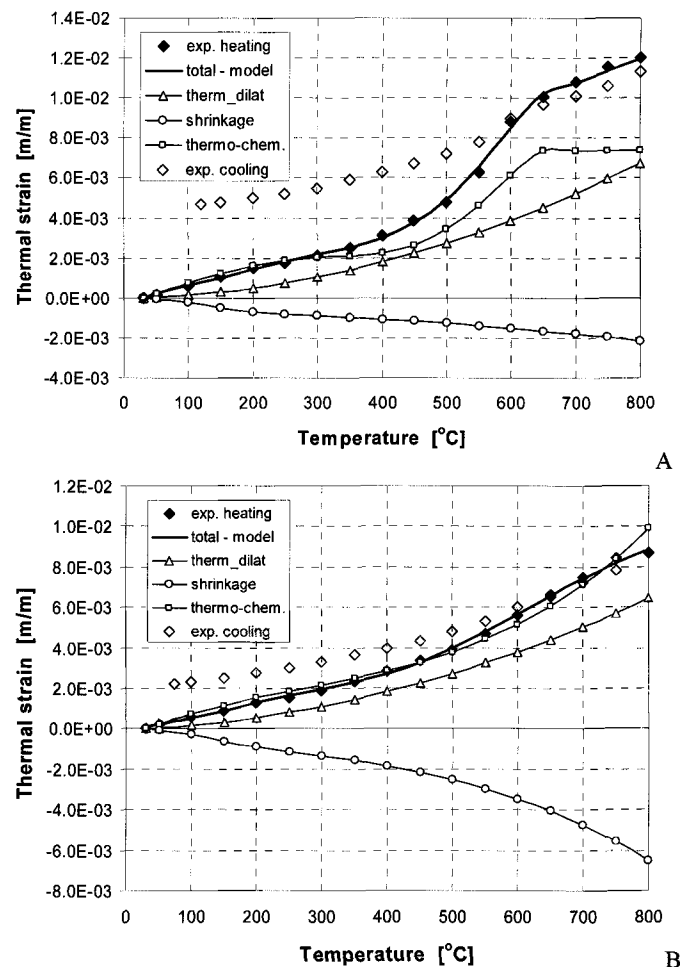

Fig. 1 - Proposed decomposition of the total thermal strain for 2 types of concrete: A) C-60, B) C-90.

Table 1 - Main properties of the C-60, C-90 and C-30 concretes at 20°C			
Material property	C-60	C-90	C-30
Water / binder ratio, w/b [-]	0.36	0.29	~0.5
Binder content, [kg/m³]	OPC: 450	OPC: 510.5 + micro-silica: 50.5	-
Aggregate type and size	calcareous, max. size of 20°mm	gabbro, max. size of 16 mm	-
MIP porosity, n [%]	9.0%	6.0%	13.7%
Water intrinsic permeability, k_o [m²]	$2.43 \cdot 10^{-18}$	$6.64 \cdot 10^{-18}$	$3.2 \cdot 10^{-17}$
Young modulus, E [GPa]	34.5	36.7	30.0
Poisson's ratio, ν [-]	0.18	0.18	0.20
Thermal conductivity, χ [W/m·K]	1.95	2.1	2.0
Specific heat, C_p [J/kg·K]	851	851	932

K_T. $x_s^{ws}(S_w)$ means the solid surface fraction in contact with the wetting film, depending on saturation degree, S_w, of the pores. We would like to underline that for porous materials with considerable internal surface of porosity, containing very fine pores, as for example concrete, x_s^{ws} is different from the saturation degree, which is usually applied in the effective stress relation, [20].

is described in our model as the thermal dilatation strain, ε_{th}, given by the following incremental relation:

$$d\varepsilon_{th} = \beta_s(T) \, dT \qquad (1)$$

with temperature dependent thermal dilatation coefficient β_s (T).

Regression analysis performed for the experimental data presented in Fig. 1 shows that a linear dependence of coefficient β_s on the temperature assures sufficient accuracy, with correlation coefficient $R^2 > 0.99$, in the whole analysed temperature range. As a result, a thermal dilatation strains can be approximated with a parabolic function of temperature.

2.2 Shrinkage strains

The initial moisture contents of both concretes (Fig. 1) corresponded to thermodynamic equilibrium with the ambient air having temperature of about 20°C and relative humidity of about 40%RH. Hence during heating and the resulting drying process one can expect considerable shrinkage strains. The latter ones were not measured in [6], but the experimental results for similar HSC, reported in [19], and our numerical simulations, based on the model presented further in this paper, allow us to estimate them at the room temperature as equal to about 400-500 μm.

Shrinkage strains are modelled here by means of the effective stress principle in the form derived in [21], which for materials with very small pores and well developed internal pore surface, where water is also present as a thin film (like for example in concrete), has the form:

$$\sigma'' = \sigma + \alpha p^s \mathbf{I}, \qquad (2)$$

where

$$p^s = p^g - x_s^{ws} p^c, \qquad (3)$$

is the solid phase pressure exerted by the pore fluids (liquid water and moist air), σ'' is the effective Bishop stress responsible for all skeleton deformations,

$$\alpha = 1 - \frac{K_T}{K_s}, \qquad (4)$$

is the Biot coefficient accounting for different values of bulk moduli for solid phase and the whole medium, K_s and

Capillary pressure takes into account water-gas interface curvature and water film effects:

$$p^c = p^g - p^w \qquad (5)$$

and for low moisture contents, when no capillary water is present in the pores, it has to be interpreted as the adsorbed water potential multiplied by the water density, [15]. Thermodynamic definition of the capillary pressure is given in Appendix.

The water film pressure, p^w, differs from the reservoir water pressure, p_o^w, by an amount equal to the disjoining pressure, Π^w, [21]:

$$p^w = p_o^w - \Pi^w. \qquad (6)$$

In Equation (3) curvature effects of water-solid and solid-gas interfaces, taken into account in [21], are omitted as being of minor importance for concrete.

Hence, an increment of the shrinkage strains, $d\varepsilon_{sh}$, can be calculated from the following expression:

$$d\varepsilon_{sh} = \frac{\alpha}{K_T}\left(dx_s^{ws} p^c + x_s^{ws} dp^c\right)\mathbf{I}. \qquad (7)$$

During heating of a load-free sample, at temperatures exceeding about 120°C, gradual degradation of concrete strength properties due to complicated thermo-chemo-mechanical processes is observed, see e.g. [4-6]. They cause a considerable decrease of the material bulk modulus, K_T, what can be described by means of the thermo-chemical damage parameter, V, introduced in [17]. It is defined in terms of the experimentally determined evolution of Young's modulus of mechanically undamaged material (i.e. heated to a given temperature, without any additional mechanical load), E_o, expressed as a function of temperature,

$$V(T) = 1 - \frac{E_o(T)}{E_o(T_a)} \qquad (8)$$

where $T_a = 20°C$ is room temperature. The parameter takes into account both effects of concrete dehydration (chemical component) and material cracking (mechanical component) on material degradation and the Young's modulus decrease with increasing temperature. Application of the parameter V
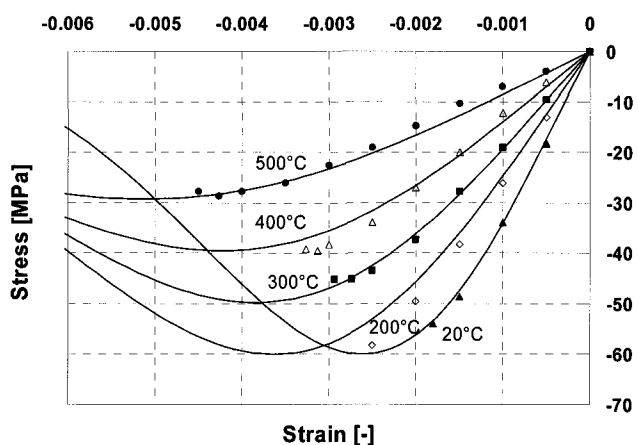
220

Fig. 2 - Comparison of the strain – stress curves at elevated temperatures for the C-60 HSC. Points represent the experimental data and thin lines correspond to theoretical relation.

in the framework of the isotropic damage theory [22-24] allows for a realistic description of strain-stress curves of concrete at high temperature [17]. The curves obtained by means of the damage theory for the C-60 HPC are presented in Fig. 2, showing a good agreement with experimental data. The damage theory will be briefly discussed in the next section.

Thus, the bulk modulus of load-free concrete at temperature T is given by

$$K_T(T) = [1 - V(T)] K_T(T_a), \qquad (9)$$

what at high temperature causes an additional increase of shrinkage strains as a result of material thermo-chemical deterioration, as was underlined in [3], see "shrinkage" line in Fig. 1. The solid phase bulk modulus K_s is also decreasing at high temperature due to dehydration and because of lack of sufficient experimental data we shall assume that Biot's coefficient α remains constant in these conditions. This means physically that K_s is affected by high temperature in a similar way like the modulus of the whole medium, Equation (9).

An important question arising from the proposed description of shrinkage phenomenon is its applicability in the high temperature range, especially above the critical point of water, where no capillary water is present in pores of the material. However, one should remember that physically adsorbed water in form of thin films still exists in these conditions, what is taken into account in Equations (2)-(6), thus the proposed formulation is also valid at high temperature. The latter conclusion is confirmed by the analysis of results of very accurate thermal dilation tests of cement pastes (to minimize effect of cracking), e.g. presented in [6]. They do not exhibit any visible changes of material behaviour (for the thermal strains and their rates) in the temperature range close to the critical point of water, where considerable chemical shrinkage strains occur too, and in particular no rapid nor gradual diminishing of shrinkage strains can be observed.

One should underline that shrinkage strains do not appear explicitly in the equation of mechanical equilibrium (27) in our model of concrete at high temperature, but shrinkage deformation is taken into account by means of the Bishop effective stresses given by (2). Equation (7) is

used only to determine the thermo-chemical strains described in the next subsection.

2.3 Thermo-chemical strains

In heated concrete, above the temperature of about 105°C, starts the thermal decomposition of the cement matrix, and at higher temperatures also of aggregate (depending on its type and composition). This is a consequence of several complicated, endothermic chemical reactions, e.g. [3], called concrete dehydration. As their result a considerable shrinkage of cement matrix (called chemical shrinkage) and usually expansion of aggregate are observed. Due to these contradictory behaviour of the material components, cracks of various dimensions are developing when temperature increases, see e.g. [6], causing an additional change of concrete strains (usually expansion).

It is practically impossible to separate effects of dehydration and cracking processes during experimental investigations of thermal dilatation of concrete or cement paste at high temperature. Further, due to the very complicated physicochemical nature of the considered phenomena, which are strongly non-linear and dependent on several factors, there is lack of a sufficiently accurate theoretical model to describe them. The only reasonable solution seems to be a direct application of experimental results, after an appropriate elaboration and interpretation.

In our model we define an increment of the thermo-chemical strain, $d\varepsilon_{tchem}$, as follows:

$$d\varepsilon_{tchem} = d\varepsilon_{tot} - d\varepsilon_{sh} - d\varepsilon_{th} \qquad (10)$$

where $d\varepsilon_{tot}(0,T)$ is an increment of the total, experimentally measured strain of load-free material (zero means value of the mechanical stress), while $d\varepsilon_{sh}(T)$ and $d\varepsilon_{th}(T)$ are determined from (1) and (7).

The physical nature of the strain (10) suggests that it should be related to the thermo-chemical damage parameter. Indeed, our extensive investigations of experimental results for several types of concrete show that there is a direct and theoretically sound dependence of the thermo-chemical strain $\varepsilon_{tchem}(T)$ upon the thermo-chemical damage parameter $V(T)$. Then, for the analysed concretes, the latter one was also correlated with the dehydration degree (Fig. 4) describing advancement of chemical decomposition and defined as:

$$\Gamma_{dehydr}(T) = \frac{m(T_o) - m(T)}{m(T_o) - m(T_\infty)}, \qquad (11)$$

where $m(T)$ is mass of concrete sample measured at temperature T during thermo-gravimetric tests, T_o and T_∞ are temperatures when the dehydration process starts and finishes. We assumed here $T_o = 105°C$ and $T_\infty = 1000°C$.

As an illustration of the aforementioned relations, we present in Figs. 3-5 some experimental data for C-60 concrete. Fig. 3a shows the results of thermo-gravimetric (TG) tests and their interpretation in terms of the dehydration degree, Γ, and Fig. 3b contains similar data but for the Young modulus and the thermo-chemical damage parameter, V. A correlation between the experimental values and the approximated relations for both the
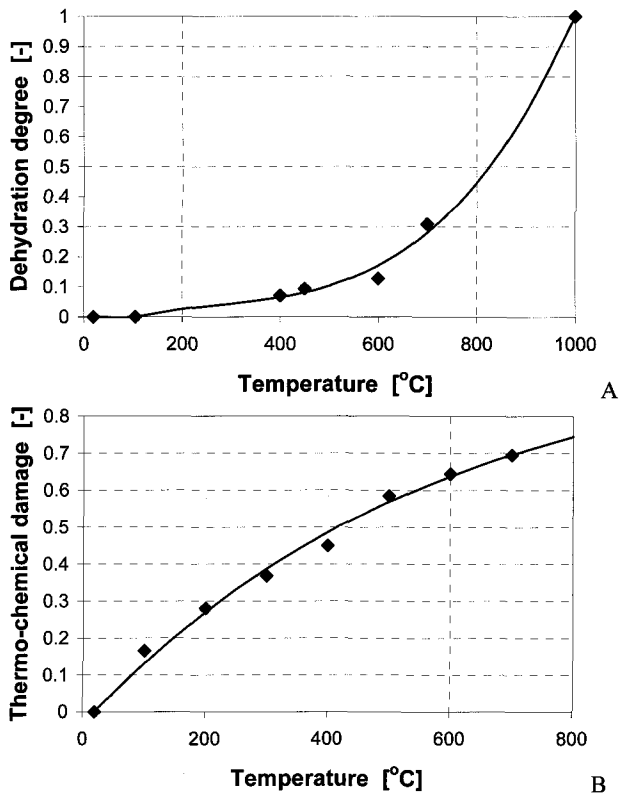
Fig. 3 - Experimental data for the C-60 HSC and their approximations used in our model: A) TG test results expressed as dehydration degree; B) Young's modulus measurements in terms of thermo-chemical damage.
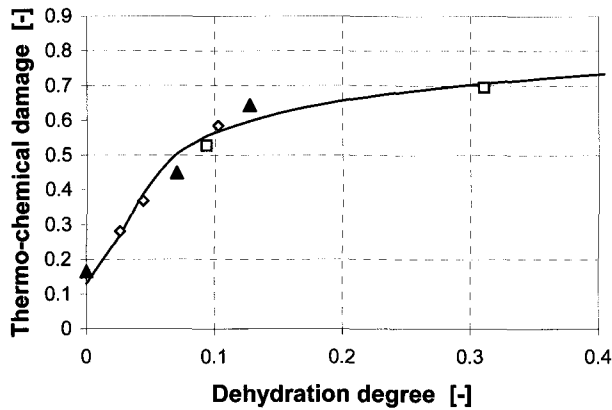

Fig. 4 - Correlation between results of the TG tests and strength measurements for the C-60 HSC expressed in terms of dehydration degree and thermo-chemical damage parameter.

dehydration degree and the thermo-chemical damage parameter is visible in Fig. 4. The black triangles indicate points for temperatures, where data both for Γ and V were determined; squares: points where only values of Γ were measured and for the other parameter the approximated formula was used; and for diamonds: vice-versa, only values of V were measured. Up to temperature of about 500÷550°C ($\Gamma \cong 0.1÷0.12$) thermo-chemical damage increases more rapidly with the advancement of dehydration process (concerning mainly the cement matrix), what corresponds to the temperature range where thermal decomposition of CSH (105÷600°C) and portlandite (400÷450°C) phases of cement paste takes
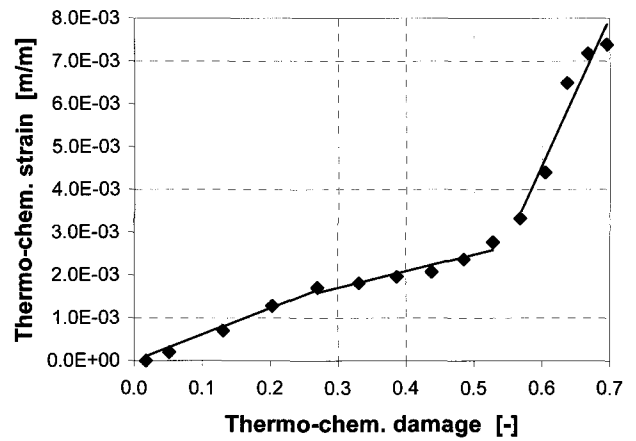

Fig. 5 - Relation between the thermo-chemical strains measured for the C-60 concrete at various temperatures and the corresponding values of thermo-chemical damage parameter. Thin lines indicate three ranges of different (approximately linear) thermo-chemical strain-damage behaviour.

place, [6]. Above this temperature starts decomposition of the calcareous aggregate and the rate of thermo-chemical deterioration is visibly smaller. This phenomenon is more evident in Fig. 5, showing evolution of thermo-chemical strain, defined by (10), for increasing value of the thermo-chemical damage parameter. After this parameter has reached the value of about 0.55, corresponding to the beginning of the aggregate thermo-chemical decomposition, a much more rapid increase of thermo-chemical strains is observed.

This clearly shows that the adopted model of concrete dehydration, degradation of its strength properties and resulting deformations at high temperature takes into account the mutual couplings between these thermo-chemical and mechanical processes. For these reasons we define a constitutive relationship for the thermo-chemical strain increment in the form:

$$d\varepsilon_{tchem} = \beta_{tchem}(V)dV,\qquad(12)$$

where $\beta_{tchem}(V) = \dfrac{\partial \varepsilon_{tchem}(V)}{\partial V}$ is obtained from experimental tests, see e.g. Fig. 5.

The components of LFTS, resulting from our model, and their sum are compared in Fig. 1 with the measured values of the total thermal strains for two types of concrete, [6]. A much higher values of shrinkage (obtained from numerical simulation) for the C-90 HSC are caused by much faster evolution of the thermo-chemical damage of this material at high temperature ($V\cong0.9$ at T=700°C), as compared to the C-60 concrete ($V\cong0.7$ at T=700°C), Fig. 3b.

3. MODELLING LITS OF MECHANICALLY LOADED CONCRETE AT HIGH TEMPERATURE

During first heating, mechanically loaded concrete exhibits greater strains as compared to the load-free material at the same temperature. These additional deformations are referred to as load induced thermal strains (LITS) [18]. A part of them originates just from the elastic deformation due to mechanical

load, $\varepsilon_{el}(\sigma,T)$, and it increases during heating because of thermo-chemical and mechanical degradation of the material strength properties. The time dependent part of the strains during transient thermal processes due to temperature changes, $\varepsilon_{tr}(\sigma,T)$, is generally called thermal creep. Its physical nature is rather complicated and up today not fully understood, thus modelling is usually based on the results of special experimental tests. Typically, they are performed at constant heating rate equal to 2 K/min, for various (but constant during a particular test) levels of material stresses, σ=const, ranging from 0% (load-free measurements) to 60% of the compressive strength of material at room temperature, $f_c(T_a)$. The results of such transient thermal strain tests performed for the C-60 concrete are presented in Fig. 6, where experimental data [6] are shown as diamond points.

LITS can be calculated from these results as the difference of total strains for loaded and unloaded samples of concrete at a given temperature, $\varepsilon_{tot}(\sigma,T)$ and $\varepsilon_{tot}(0,T)$, and transient thermal strains, $\varepsilon_{tr}(\sigma,T)$, by additional subtracting from LITS the elastic part of mechanical deformations $\varepsilon_{el}(\sigma,T)$ (usually at room temperature, $T=T_a$). The obtained values, after division by the load factor (ratio of the actual material stress σ to the ultimate stress value at room temperature, $f_c(T_a)$) are typically presented in the form of the normalised transient strain curves, Fig. 7.
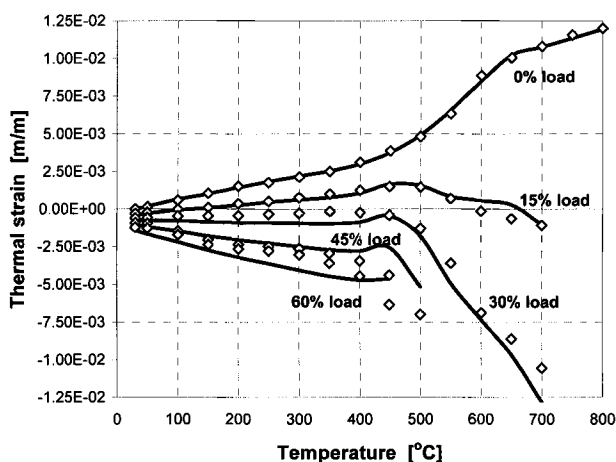

Fig. 6 - Comparison of the results of thermal transient strains measurements for the C-60 HSC [6] and values obtained from our model (thin lines).
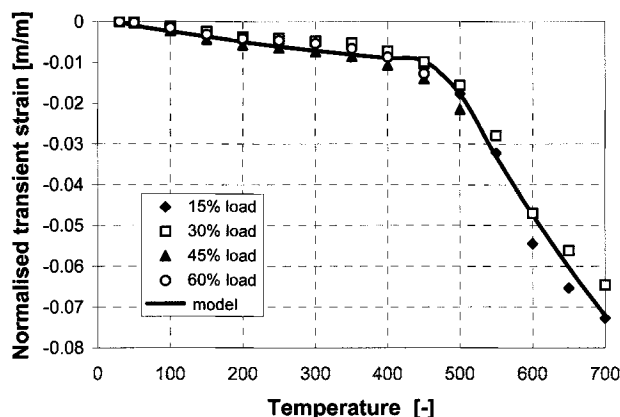

Fig. 7 - Comparison of the measured normalized thermal transient strains for the C-60 HSC [6] and their approximation used in our model.

At this point we will briefly discuss elastic mechanical deformations of concrete and its stress-strain behaviour at high temperature, which are presented in more detail in [17]. These elements are necessary for a proper analysis and decomposition of LITS.

Concrete is a brittle material with different mechanical characteristics in compression and tension, and moreover, it exhibits strain softening after exceeding stress level corresponding to its strength. For realistic description of its mechanical performance a non-linear theory is necessary. As already mentioned in previous section, we describe mechanical behaviour of concrete, taking into account thermo-chemical and mechanical degradation, following the scalar isotropic damage model by Mazars [22-24]. In this model, the damaged material at given temperature, T, is supposed to behave elastically and to remain isotropic. Its Young's modulus at this temperature, $E(T)$, can be obtained from the value of mechanically undamaged material at the same temperature, $E_o(T)$, [22-24], and mechanical damage parameter, d, defined as

$$d = 1 - \frac{E(T)}{E_o(T)}. \tag{13}$$

This parameter can be treated as a measure of cracks' volume density in the material.

A total effect of the mechanical and thermo-chemical damages, to which the material is exposed at the same time, is multiplicative, *i.e.* the total damage parameter, D, is defined by the following formula,

$$D = 1 - \frac{E(T)}{E_o(T_a)} = 1 - \frac{E(T)}{E_o(T)}\frac{E_o(T)}{E_o(T_a)}$$
$$= 1 - (1-d)\cdot(1-V) \tag{14}$$

and not just by the sum of the two components of damage.

Therefore, the classical effective stress concept, [25], is modified to take into account both the mechanical and thermo-chemical damage, so a further reduction of resistant section area due to thermo-chemical degradation is added to that caused by the mechanical damage, *i.e.* the section reduction by cracking:

$$\tilde{\sigma} = \sigma''\frac{S}{\tilde{S}} = \frac{\sigma''}{(1-d)(1-V)}, \tag{15}$$

where S and $\tilde{S}$ mean total and resistant area of the damaged material, σ'' is the Bishop effective stress tensor and $\tilde{\sigma}$ the tensor of the "net" effective stress (in the sense of Mazars [22-23]).

The stress-strain curves of concrete at high temperature, resulting from the described theory are shown in Fig. 2. During heating of a concrete sample loaded at constant stress level, as is usually done during transient thermal creep tests, mechanical strains of the material are gradually increasing following the "growing" branches of the "σ-ε" curves, where the mechanical damage parameter d is equal to zero. Only at higher temperatures, when stress level is closer to the compressive strength and the curves exhibit some non-linearity, the mechanical damage parameter reaches some small value. But soon after that, at temperatures when the stress level equals the compressive strength, the sample is destroyed and the test finishes. Thus,

except for a small "final" part of the temperature-LITS curve, see *e.g.* Fig. 6, one can assume that the mechanical damage parameter equals zero, $d=0$.

Hence only thermo-chemical damage is considered during calculation of the elastic mechanical strains at given temperature, which are needed to evaluate the transient thermal strains. To find them, we follow a commonly used approach, but taking additionally a change of the concrete bulk modulus due to thermo-chemical degradation into account. In this way we avoid considering the same temperature-related strains twice, what happens when elastic mechanical strains are assumed constant and equal to their value at initial temperature.

The total strain of a mechanically loaded concrete at temperature T, where the "net" effective stress due to external load and pressure of pore fluids (*i.e.* liquid water and moist air) equals to $\tilde{\sigma}$, consists of the following components:

$$\varepsilon_{tot}(\tilde{\sigma},T) = \varepsilon_{tr}(\tilde{\sigma},T) + \varepsilon_{el}(\tilde{\sigma},T) \\ + \varepsilon_{tchem}(V(T)) + \varepsilon_{th}(T) \cdot \tag{16}$$

One must remember that the shrinkage strain ε_{sh} is included into the elastic strain component ε_{el} as a result of action of capillary pressure or disjoining pressure upon the solid surface fraction $x_s^{ws}(S_w)$, dependent on the moisture content.

Thus, for 1D case the normalized thermal transient strain $\overline{\varepsilon}_{tr}(T)$, at temperature T, can be found from the formula:

$$\overline{\varepsilon}_{tr}(T) = \overline{\varepsilon}_{tr}(V(T)) = \\ \left[\varepsilon_{tot}(\tilde{\sigma},T) - \varepsilon_{tot}(0,T) - \frac{\varepsilon_{el}(\tilde{\sigma},T_a)}{1-V(T)} \right] \frac{f_c(T_a)}{\tilde{\sigma}(T)} \cdot \tag{17}$$

The results obtained following the presented approach for the C-60 concrete, indicate that the transient thermal strains are, in general, proportional to the material effective stress levels, see Fig. 7. To define a constitutive relationship for transient thermal strains we use the curves obtained by means of the least square method from the experimental data for the all considered load levels, Fig. 7. One must remember that the curves were obtained for the heating rate of 2 K/min, but we assume that they are valid for any heating rate, because LITS depends mainly on the temperature increment (and the corresponding thermo-chemical damage increment) and not the temperature rate.

Analysis of the results presented in Fig. 7 shows that the transient strain behaviour changes significantly in the temperature range of 450-500°C (corresponding to thermo-chemical damage $V\cong0.55$, Fig. 8). An interesting point is that in the same temperature range also behaviour of the unloaded material changes (see the thermo-chemical strain in Fig. 5 and the thermo-chemical damage in Fig. 4). This is a result of very advanced thermo-chemical decomposition of cement matrix (CSH and portlandite) and beginning of decomposition of the calcareous aggregate, connected with micro-cracks and cracks development. It shows again the importance of some mutual couplings between thermo-chemical and thermo-mechanical phenomena at high temperature, what should be properly taken into account in
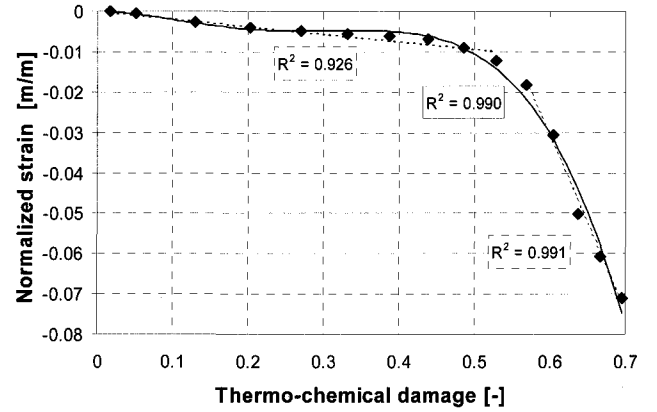

Fig. 8 - Correlation between of the measured normalized thermal transient strains and thermo-chemical damage values for the C-60 HCS (data from [6]).

the choice of the state variables and formulation of constitutive relationships. It also suggests that all the aforementioned thermo-physicochemical phenomena have, at least in part, common physical origins (*i.e.* dehydration and material cracking) and are correlated with the evolution of thermo-chemical damage parameter, V, as shown in Fig. 8 (correlation coefficients R^2 for polynomial and bilinear approximations are given on the graph). Moreover, the latter parameter is irreversible, as the transient thermal strains are [34]. This suggests that the strains should be expressed in terms of thermo-chemical damage - V, rather than temperature - T, what was previously used in some models, *e.g.* [11, 34-36]. This allow us to avoid additional checking, whether the thermo-chemical damage is increasing, what was necessary for example in the model proposed in [36].

In our model the transient thermal strain increments are obtained from the derivative of $\overline{\varepsilon}_{tr}(V)$ with respect to thermo-chemical damage, V, using the following formula:

$$d\varepsilon_{tr} = \frac{\partial \overline{\varepsilon}_{tr}(V)}{\partial V} \frac{\tilde{\sigma}}{f_c(T_a)} dV = \overline{\beta}_{tr}(V) \frac{\tilde{\sigma}}{f_c(T_a)} dV \tag{18}$$

Thanks to the shape of the $\overline{\varepsilon}_{tr}(V)$ curve, Fig. 8, a simplified, bilinear relation for $\overline{\beta}_{tr}(V)$ may be used (slopes of the dotted lines in Fig. 8) or its polynomial approximation (derivatives of the curve in Fig. 8). The bilinear relation clearly shows a qualitative change of the material behaviour above the temperature $T> 470°C$ and after integration it gives a good approximation of the LITS, Fig. 6.

Equation (18) has been generalised to a multi-axial stress state similarly as in [11, 35, 36], resulting in the following formula:

$$d\varepsilon_{tr} = \frac{\overline{\beta}_{tr}(V)}{f_c(T_a)} \mathbf{Q} : \tilde{\sigma} \, dV \cdot \tag{19}$$

where $\mathbf{Q}$ is a fourth order tensor defined as follows:

$$Q_{ijkl} = -\gamma\delta_{ij}\delta_{kl} + \frac{1}{2}(1+\gamma)(\delta_{ik}\delta_{jl} + \delta_{il}\delta_{jk}), \tag{20}$$

with γ being a material parameter determined from the transient creep test.

Application of the proposed model of the transient thermal strains, applied for the C-60 concrete, for four different levels of compressive loads, gives satisfactory predictions of LITS as may be seen in Fig. 6. LFTS have been evaluated using the model presented in the previous section. Some visible discrepancies between theoretical and experimental results are due to some non-linear effects, probably related to stress level, and possible inaccuracy of strains measurements, as well as difficulties in maintaining really constant heating rate and stress level during the tests.

4. MODEL OF HYGRO-THERMO-CHEMO-MECHANICAL PERFORMANCE OF CONCRETE AT HIGH TEMPERATURE

The model of deformations of concrete at high temperature, described in previous sections, has been introduced into the mathematical model of hygro-thermal behaviour and chemo-mechanical degradation of concrete at high temperature which was originally proposed in [9, 14, 15, 17].

For convenience we briefly summarize now the main assumptions and equations of the whole model, taking into account the modifications introduced in this paper.

The equations of the model are written by considering concrete as a multi-phase material, with the solid skeleton voids filled partly by liquid water and partly by a gas phase.

Below the critical temperature of water, T_{cr}, the liquid phase consists of bound water and capillary water, which appears when the degree of water saturation exceeds the upper limit of the hygroscopic region, S_{ssp}. Above the temperature T_{cr} the liquid phase consists of bound water only. In the whole temperature range the gas phase is a mixture of dry air and water vapour, which is a condensable gas constituent for temperatures $T<T_{cr}$.

The model equations are obtained by means of the Hybrid Mixture Theory (HMT), [26-30], and their full development, starting from the local, microscopic balance equations with successive volume averaging, as well as their weak (integral) formulation are presented in [31, 32]. Thermal, chemical (dehydration) and mechanical degradation of concrete at high temperature are described by means of the non-local, isotropic scalar damage theory, [22-24], appropriately modified in [17].

To describe uniquely the state of concrete at high temperature, we need 4 primary state variables, *i.e.* gas pressure, p^g, capillary pressure, p^c, temperature, T, and displacement vector, $\mathbf{u}$, as well as 3 internal variables describing advancement of the dehydration and deterioration processes, *i.e.* degree of dehydration, Γ_{dehydr}, chemical damage parameter, V, and mechanical damage parameter, d.

The model consists of 7 equations: 2 mass balances (continuity equations), enthalpy (energy) balance, linear momentum balance (mechanical equilibrium equation) and 3 evolution equations. The final form of the model equations, expressed in terms of the primary state variables, after introducing the constitutive relationships are listed below (the symbols used are explained in the Nomenclature). The full development of the equations is presented in [17].

Mass balance equation of the dry air (involving the solid skeleton mass balance) takes into account both diffusive and advective air flow, as well as variations of porosity caused by dehydration process and deformations of the skeleton. It has the following form:

$$-n\rho^{ga}\left(\frac{\partial S_w}{\partial T}\frac{\partial T}{\partial t}+\frac{\partial S_w}{\partial p^c}\frac{\partial p^c}{\partial t}\right)$$

$$-\beta_s\rho^{ga}\left(1-n\right)\left(1-S_w\right)\frac{\partial T}{\partial t}$$

$$+\left(1-S_w\right)\rho^{ga}\,div\frac{\partial\mathbf{u}}{\partial t}+\left(1-S_w\right)$$

$$n\left(\frac{\partial\rho^{ga}}{\partial T}\frac{\partial T}{\partial t}+\frac{\partial\rho^{ga}}{\partial p^c}\frac{\partial p^c}{\partial t}+\frac{\partial\rho^{ga}}{\partial p^g}\frac{\partial p^g}{\partial t}\right)$$

$$-div\left[\rho^g\frac{M_aM_w}{M_g^2}\mathbf{D}_d^{ga}\,grad\left(\frac{p^{ga}}{p^g}\right)\right]$$

$$+div\left\{\rho^{ga}\frac{kk^{rg}}{\mu^g}\left[-grad\,p^g+\rho^g\mathbf{g}\right]\right\}$$

$$=\frac{\rho^{ga}}{\rho^s}\left(1-S_w\right)\left[\dot{m}_{dehydr}+\left(1-n\right)\frac{\partial\rho^s}{\partial\Gamma_{dehydr}}\frac{\partial\Gamma_{dehydr}}{\partial t}\right]$$

$$(21)$$

Mass balance equation of the water species (involving the solid skeleton mass balance) considers diffusive and advective flow of water vapour, mass sources related to phase changes of vapour (evaporation-condensation, physical adsorption - desorption and dehydration), and variations of porosity caused by dehydration process and deformations of the skeleton, resulting in the following equation:

$$n\left(\rho^w-\rho^{gw}\right)\left(\frac{\partial S_w}{\partial T}\frac{\partial T}{\partial t}+\frac{\partial S_w}{\partial p^c}\frac{\partial p^c}{\partial t}\right)$$

$$+\left[\rho^wS_w+\rho^{gw}\left(1-S_w\right)\right]div\frac{\partial\mathbf{u}}{\partial t}$$

$$+\left(1-S_w\right)n\left(\frac{\partial\rho^{gw}}{\partial T}\frac{\partial T}{\partial t}+\frac{\partial\rho^{gw}}{\partial p^c}\frac{\partial p^c}{\partial t}\right)$$

$$-div\left[\rho^g\frac{M_aM_w}{M_g^2}\mathbf{D}_d^{gw}grad\left(\frac{p^{gw}}{p^g}\right)\right]$$

$$+div\left\{\rho^{gw}\frac{kk^{rg}}{\mu^g}\left[-grad\,p^g+\rho^g\mathbf{g}\right]\right\}-\beta_{swg}\frac{\partial T}{\partial t}$$

$$+div\left\{\rho^w\frac{kk^{rw}}{\mu^w}\left[-grad\,p^g+grad\,p^c+\rho^w\mathbf{g}\right]\right\}=$$

$$+\frac{\rho^wS_w+\rho^{gw}\left(1-S_w\right)}{\rho^s}$$

$$\left[\left(1-n\right)\frac{\partial\rho^s}{\partial\Gamma_{dehydr}}\frac{\partial\Gamma_{dehydr}}{\partial t}+\dot{m}_{dehydr}\right]-\dot{m}_{dehydr},$$

$$(22)$$

with β_{swg} defined by:

$$\beta_{swg} = \beta_s \left(1 - n\right)\left(S_g \rho^{gw} + S_w \rho^w\right) + n\,\beta_w S_w \rho^w$$
$$(23)$$

Enthalpy balance equation of the multi-phase medium, accounting for the conductive and convective heat flow, and heat effects of phase changes and dehydration process, can be written as follows:

$$\left(\rho C_p\right)_{eff} \frac{\partial T}{\partial t} + \rho^w C_p^w$$

$$\left\{\frac{kk^{rw}}{\mu^w}\left[-grad\,p^g + grad\,p^c + \rho^w \mathbf{g}\right]\right\} \cdot grad\,T$$

$$+\rho^g C_p^g \left\{\frac{kk^{rg}}{\mu^g}\left[-grad\,p^g + \rho^g \mathbf{g}\right]\right\} \cdot grad\,T$$

$$-div\left(\chi_{eff}\,grad\,T\right)$$

$$= -\dot{m}_{vap}\,\Delta H_{vap} - \dot{m}_{dehydr}\,\Delta H_{dehydr}$$
$$(24)$$

where the water vapour source term is given by:

$$\dot{m}_{vap} = -\rho^w S_w\,div\frac{\partial \mathbf{u}}{\partial t} + \beta_{sw}^* \rho^w \frac{\partial T}{\partial t}$$

$$-\rho^w n\left(\frac{\partial S_w}{\partial T}\frac{\partial T}{\partial t} + \frac{\partial S_w}{\partial p^c}\frac{\partial p^c}{\partial t}\right)$$

$$-div\left[\rho^w \frac{k\,k^{rw}}{\mu^w}\left(-grad\,p^g + grad\,p^c + \rho^w \mathbf{g}\right)\right] +$$

$$-\left(\dot{m}_{dehydr} + \left(1 - n\right)\frac{\partial \rho^s}{\partial \Gamma_{dehydr}}\frac{\partial \Gamma_{dehydr}}{\partial t}\right)\frac{\rho^w S_w}{\rho^s} + \dot{m}_{dehydr}$$
$$(25)$$

with $\beta_{sw}^* = S_w\left[\left(1 - n\right)\beta_s + n\beta_w\right]$,

and the dehydrated water source is proportional to the dehydration rate:

$$\dot{m}_{dehydr} = k_b\,\dot{\Gamma}_{dehydr},$$
$$(26)$$

k_b is a material parameter related to the chemically bound water and dependent on the stoichometry of the chemical reactions associated to dehydration process.

Linear momentum conservation equation of the multi-phase medium, has the following form:

$$div\left(\mathbf{\sigma}'' - \alpha p^s\,\mathbf{I}\right) + \rho \mathbf{g} = 0,$$
$$(27)$$

where the effective stresses $\mathbf{\sigma}''$ is given by:

$$\mathbf{\sigma}'' = (1 - d)(1 - V)\Lambda_0 : \left(\mathbf{\varepsilon}_{tot} - \mathbf{\varepsilon}_{th} - \mathbf{\varepsilon}_{tchem} - \mathbf{\varepsilon}_{tr}\right),$$
$$(28)$$

where thermal strain $\mathbf{\varepsilon}_{th}$ is obtained from (1), thermo-chemical strain $\mathbf{\varepsilon}_{tchem}$ from (10), and transient thermal strain $\mathbf{\varepsilon}_{tr}$ from (18).

Dehydration process evolution law, considering its irreversibility, obtained from experiments, *e.g.* TG or DTA tests, has the form:

$$\Gamma_{dehydr}\left(t\right) = \Gamma_{dehydr}\left(T_{max}\left(t\right)\right),$$
$$(29)$$

thus

$$\dot{\Gamma}_{dehydr} = \frac{\partial \Gamma_{dehydr}\left(t\right)}{\partial t} \quad \text{for } T(t) \geq T_{max}\left(t\right),$$

$$\dot{\Gamma}_{dehydr} = 0 \quad\quad\quad \text{for } T(t) < T_{max}\left(t\right),$$
$$(30)$$

where $T_{max}(t)$ is the highest temperature reached by the concrete up to the time instant t.

Thermo-chemical damage evolution equation, obtained from the experimental results by means of equation (8), which takes into account the irreversible character of the material structural changes may be written as:

$$V\left(t\right) = V\left(T_{max}\left(t\right)\right),$$
$$(31)$$

Mechanical damage evolution equation, $d\left(t\right) = d\left(\tilde{\varepsilon}\left(t\right)\right)$, expressed in terms of the equivalent strain, $\tilde{\varepsilon}$, is given by equations of the classical non-local, isotropic damage theory, [22-24].

For the model closure we used several *thermodynamic relations* (*e.g.* the Kelvin equation, valid because of the assumption about the local equilibrium state), *constitutive relationships* between intensive and extensive thermodynamic quantities (*e.g.* Darcy's law, Fick's law or Fourier's law, defining generalized thermodynamic fluxes of extensive variables) and *state equations* (*e.g.* Clapeyron's law of ideal gas, Dalton's law or the Hyland-Wexler equation for the saturated vapour pressure) - expressing known laws of Physics, and finally, *material functions* defining some physical properties, usually being coefficients of the constitutive relations. More details about the specific form of the material function can be found in [9, 14, 15, 17]; here we mention only, that usually they depend on several state variables, *e.g.* $k = f(p^g, T, D)$, $\mu_g = f(p^c, p^g, T)$, $S_w = f(p^c, T)$, $\chi_{eff} = f(S_w, V)$, $D_d^{gw} = f(S_w, T)$.

To solve any initial-boundary value problem, corresponding to a practical situation under consideration, we must define initial and boundary conditions. The *initial conditions* specify the full fields of primary state variables at time instant t=0, in the whole analysed domain Ω and on its boundary Γ, ($\Gamma = \Gamma_\pi \cup \Gamma_\pi^q$, $\pi = g, c, t, u$):

$$p^g = p_o^g, p^c = p_o^c, T = T_o, \mathbf{u} = \mathbf{u}_o, \quad \text{on } \left(\Omega \cup \Gamma\right),$$
$$(32)$$

The *boundary conditions* (BCs) can be of Dirichlet's type on Γ_π:

$$p^g\left(t\right) = \hat{p}^g\left(t\right) \text{ on } \Gamma_g,$$

$$p^c\left(t\right) = \hat{p}^c\left(t\right) \text{ on } \Gamma_c,$$

$$T\left(t\right) = \hat{T}\left(t\right) \text{ on } \Gamma_t,$$

$$\mathbf{u}\left(t\right) = \hat{\mathbf{u}}\left(t\right) \text{ on } \Gamma_u,$$
$$(33)$$

or of Cauchy's type (the mixed BCs) on Γ_π^q:

$$\left[n\left(1-S_w\right)\rho^{ga}\mathbf{v}^{gs} + \mathbf{J}_d^{ga} \right]\cdot\mathbf{n} = q^{ga}, \quad \text{on } \Gamma_g^q$$

$$\left[nS_w\rho^w\mathbf{v}^{ws} + n\left(1-S_w\right)\rho^{gw}\mathbf{v}^{gs} + \mathbf{J}_d^{gw} \right]\cdot\mathbf{n} =$$

$$q^{gw} + q^w + \beta_c\left(\rho^{gw} - \rho_\infty^{gw}\right), \quad \text{on } \Gamma_c^q$$

$$\left(nS_w\rho^w\mathbf{v}^{ws}\Delta H_{vap} - \chi_{eff}\,grad\,T\right)\cdot\mathbf{n} =$$ (34)

$$= q^T + \alpha_c\left(T-T_\infty\right) + e\sigma_o\left(T^4 - T_\infty^4\right), \quad \text{on } \Gamma_T^q$$

$$\boldsymbol{\sigma}''\cdot\mathbf{n} = \bar{\mathbf{t}}, \quad \text{on } \Gamma_u^q$$

where **n** is the unit normal vector, pointing toward the surrounding gas. The boundary conditions, with only imposed fluxes given, are the usual Neumann's BCs.

The governing equations of the model are discretised in space by means of the finite element method, [33]. The unknown variables are expressed in terms of their nodal values as,

$$p^g(t) \cong \mathbf{N}_p\,\overline{\mathbf{p}}^g(t), \qquad p^c(t) \cong \mathbf{N}_p\,\overline{\mathbf{p}}^c(t),$$

$$T(t) \cong \mathbf{N}_t\,\overline{\mathbf{T}}(t), \qquad \mathbf{u}(t) \cong \mathbf{N}_u\,\overline{\mathbf{u}}(t).$$ (35)

The variational or weak form of the model equations, applying also the other ones required to complete the model, was obtained in [31, 32] by means of Galerkin's method (weighted residuals), and can be written in the following concise discretised matrix form,

$$\mathbf{C}_{ij}(\mathbf{x})\frac{\partial\mathbf{x}}{\partial t} + \mathbf{K}_{ij}(\mathbf{x})\,\mathbf{x} = \mathbf{f}_i(\mathbf{x}),$$ (36)

with

$$\mathbf{K}_{ij} = \begin{bmatrix} \mathbf{K}_{gg} & \mathbf{K}_{gc} & \mathbf{K}_{gt} & 0 \\ \mathbf{K}_{cg} & \mathbf{K}_{cc} & \mathbf{K}_{ct} & 0 \\ \mathbf{K}_{tg} & \mathbf{K}_{tc} & \mathbf{K}_{tt} & 0 \\ \mathbf{K}_{ug} & \mathbf{K}_{uc} & \mathbf{K}_{ut} & \mathbf{K}_{uu} \end{bmatrix},$$

$$\mathbf{C}_{ij} = \begin{bmatrix} \mathbf{C}_{gg} & \mathbf{C}_{gc} & \mathbf{C}_{gt} & \mathbf{C}_{gu} \\ 0 & \mathbf{C}_{cc} & \mathbf{C}_{ct} & \mathbf{C}_{cu} \\ 0 & \mathbf{C}_{tc} & \mathbf{C}_{tt} & \mathbf{C}_{tu} \\ 0 & 0 & 0 & 0 \end{bmatrix}, \quad \mathbf{f}_i = \begin{Bmatrix} \mathbf{f}_g \\ \mathbf{f}_c \\ \mathbf{f}_t \\ \mathbf{f}_u \end{Bmatrix},$$ (37)

where $\mathbf{x}^T = \{\overline{\mathbf{p}}^g, \overline{\mathbf{p}}^c, \overline{\mathbf{T}}, \overline{\mathbf{u}}\}$ and the non-linear matrix coefficients $\mathbf{C}_{ij}(\mathbf{x})$, $\mathbf{K}_{ij}(\mathbf{x})$ and $\mathbf{f}_i(\mathbf{x})$ are defined in detail in [17].

The time discretization is accomplished through a fully implicit finite difference scheme (backward difference),

$$\boldsymbol{\Psi}^i\left(\mathbf{x}_{n+1}\right) = \mathbf{C}_{ij}\left(\mathbf{x}_{n+1}\right)\frac{\mathbf{x}_{n+1}-\mathbf{x}_n}{\Delta t}$$

$$+\mathbf{K}_{ij}\left(\mathbf{x}_{n+1}\right)\mathbf{x}_{n+1} - \mathbf{f}_i\left(\mathbf{x}_{n+1}\right) = \mathbf{0},$$ (38)

where superscript i ($i= g,c,t,u$) denotes the state variable, n is the time step number and Δt the time step length.

The equation set (38) is solved by means of a monolithic Newton-Raphson type iterative procedure [9, 14, 15, 17]:

$$\boldsymbol{\Psi}^i\left(\mathbf{x}_{n+1}^k\right) = -\left.\frac{\partial\boldsymbol{\Psi}^i}{\partial\mathbf{x}}\right|_{\mathbf{x}_{n+1}^k}\Delta\mathbf{x}_{n+1}^k,$$

$$\mathbf{x}_{n+1}^{k+1} = \mathbf{x}_{n+1}^k + \Delta\mathbf{x}_{n+1}^k,$$ (39)

where k is the iteration index and $\dfrac{\partial\boldsymbol{\Psi}^i}{\partial\mathbf{x}}$ is Jacobian matrix.

To solve the linear momentum balance equation numerically, it is necessary to consider the total strain tensor, the transient creep tensor and the internal variables (*i.e.* damage parameters and the degree of dehydration) at time step n (previous time step of the calculation), and the increment of strain tensor at the current step (and current iteration, k):

$$\left(\boldsymbol{\sigma}_n'', \varepsilon_{tot,n}, \varepsilon_{th,n}, \varepsilon_{tchem,n}, \varepsilon_{tr,n}, V_n, d_n, \Delta\varepsilon_{tot,n+1}\right)$$ (40)

At time step $n+1$, using backward Euler, we have the following set of local discrete equations:

$$\varepsilon_{tot,n} = \varepsilon_{tot,n+1} + \Delta\varepsilon_{tot,n+1}$$

$$\boldsymbol{\sigma}_n'' = \boldsymbol{\sigma}_{n+1}'' + \Delta\boldsymbol{\sigma}_{n+1}''$$ (41)

and taking into account the latter equations together with (2) and (15), one obtains:

$$\tilde{\boldsymbol{\sigma}}_{n+1} = \frac{\boldsymbol{\sigma}_{n+1}''}{\left(1-D_{n+1}\right)} = \tilde{\boldsymbol{\sigma}}_{n+1}^{trial} - \boldsymbol{\Lambda}_0 : \Delta\varepsilon_{tr,n+1}$$ (42)

where $\tilde{\boldsymbol{\sigma}}_{n+1}$ is the "net" stress tensor,

$$\tilde{\boldsymbol{\sigma}}_{n+1}^{trial} = \boldsymbol{\Lambda}_0 : \left(\varepsilon_{tot,n+1} - \varepsilon_{th,n+1} - \varepsilon_{tchem,n+1} - \varepsilon_{tr,n}\right)$$ (43)

is the "trial" net stress tensor, and $\Delta\varepsilon_{tr,n+1}$ is defined by (see (19) and (20)):

$$\Delta\varepsilon_{tr,n+1} = \frac{\overline{\beta}_{tr}\left(V_{n+1}\right)}{\mathrm{f}_c\left(T_a\right)}\Delta V_{n+1}\mathbf{Q} : \tilde{\boldsymbol{\sigma}}_{n+1}.$$ (44)

Considering (44), equation (42) can be written as:

$$\tilde{\boldsymbol{\sigma}}_{n+1} = \mathbf{H}_{n+1}^{-1} : \tilde{\boldsymbol{\sigma}}_{n+1}^{trial}$$ (45)

where:

$$\mathbf{H}_{n+1} = \mathbf{I} + \frac{\overline{\beta}_{tr}\left(V_{n+1}\right)}{\mathrm{f}_c\left(T_a\right)}\Delta V_{n+1}\boldsymbol{\Lambda}_0 : \mathbf{Q}$$ (46)

A two-stage solution strategy has been applied at every time step to take into account damage of concrete. First an intermediate problem, keeping the mechanical damage value constant and equal to that obtained at the previous time step, is solved. Then, the "final" solution is obtained, for all state variables and total damage parameter, by means of the modified Newton-Raphson method, using the tangential or Jacobian matrix from the last iteration of the first stage. This allowed us to avoid differentiation with

respect to the damage and to obtain a converging solution, [9, 14, 15, 17].

Because of different physical meaning of the capillary pressure p^c and different nature of the physical phenomena above the temperature T_{cr}, [15, 17], we have introduced a special 'switching' procedure [15]. When in an element part of its nodes have temperature above T_{cr}, the capillary pressure is blocked at the previous value, until the temperature in all the nodes passes the critical point of water. Then equations valid for temperature range $T > T_{cr}$ are applied in all nodes of this element.

Table2 - Concrete mixtures				
Property	MIX1	MIX2	MIX3	MIX4
Water/Cement ratio	0.22	0.33	0.33	0.57
Silica fume (% cement replacement by mass)	10	10	-	-
Final compressive strength [MPa]	98	81	72	47

5. NUMERICAL EXAMPLE

This example deals with a comparison between numerical results, obtained using the model described in the previous sections, and experimental results, obtained from compressive tests carried out in United States in the laboratories of NIST (*i.e.* National Institute of Standard and Technology) [4, 5, 12, 16]. The main goal of this comparison is to show the capability of the code to assess spalling phenomena, in particular occurrence of explosive spalling in concrete structures subjected to elevated temperatures.

Nowadays, two different approaches are used for explaining such a kind of phenomena: pore pressure based approach and purely thermo-mechanical approach.

In the first approach pore pressure is the main responsible for the explosive spalling and in particular the so-called "moisture clog" phenomenon, also known as "saturation plug", [2-17]. In a concrete element exposed to fire conditions a moving front, and four well defined zones, may be observed [2]. The first one, close to the heated surfaces, is almost completely dry and has an increasing temperature. In the second one, in the internal part of the heated element, both moisture content and temperature are at the beginning almost unchanged and their values correspond to the initial state of the material. Between these zones, there is an area with high gradients of temperature and vapour pressure, causing considerable flux of water vapour, which condensates in the cooler layer of concrete, what results in an increased moisture content inside the concrete element, close to the moving front. When temperature reaches values close to the critical point of water, an additional increase of water degree of saturation, caused by considerable thermal dilatation of the liquid water, is observed. The last two phenomena cause the "moisture clog", and are a reason of existence of the fourth zone, where moisture content is higher than the initial one, and where even fully saturated conditions may be sometimes encountered.

In the second approach spalling is due to the restrained thermal dilatation close to the heated surface, which leads to compressive stresses parallel to this surface. These compressive stresses are released by brittle fracture of concrete, resulting in the spalling process, while the role played by the pore pressure is considered secondary, [1, 3, 7, 8].

In the model presented in this work, the chosen approach takes into account both of these aspects, considering their coupling and synergic effects, *i.e.* an increase of the stresses due to high vapour pressure, and an increase of material permeability caused by the material cracking due to tensile stresses and the damage linked to these stresses, what allow us to analyse physical phenomena involved and predict the material response more correctly.

The main aim of the tests carried out at NIST laboratories was to evaluate the thermo-mechanical behaviour of concrete exposed to high temperature, in particular the estimation of Young's modulus and compressive strength as function of temperature for four different types of High Performance Concrete (HPC) characterized by different mix designs (see Table 2). The specimens, all of them were cylinders with diameter of 100mm and height of 200mm, have been tested using three test methods, representing the thermo-mechanical loading conditions: stressed test method (specimens were preloaded, with a load equal to 40% of final compressive strength at room temperature, and then heated), unstressed test method (specimens were directly heated until the time of compressive test), residual property test method (the specimens were heated up to the target temperature and kept at this temperature for a certain period; then they were cooled and tested at room temperature, *i.e.* at residual conditions).

Five target temperatures: 100°C, 200°C, 300°C, 450°C and 600°C were reached during the tests by means of furnace heating rate of 5°C/min, in steady state conditions. In this case "steady state" is defined as the temperature state when the temperature at the centre of the specimen is within 10°C of the pre-selected target temperature T and the difference between the surface and centre temperatures of the concrete specimen is less than 10°C.

For further details concerning mix compositions and tests procedures (set-up, instrumentation of the specimens, temperature control), see [4, 5, 12, 16].

Our attention was focused on specimens made of concrete type 1 and 2, herein indicated as MIX1 and MIX2, in unstressed conditions with a target temperature equal to 450°C.

In fact, for unstressed tests, explosive spalling occurred in all MIX1 specimens and in one of the four MIX2 specimens being heated to 450°C, while no spalling was observed in MIX3 and 4 up to this temperature level. All specimens in mixtures 2 and 3 that were being heated to 600°C also failed due to explosive spalling. Mixture 1 was not tested at 600°C due to the consistent spalling failure observed at the lower temperature of 450°C. MIX4 specimens did not experience any spalling failure throughout the entire temperature range.

Initial and boundary conditions used in numerical simulation are listed in Tables 3 and 4.

Fig. 9 shows for MIX1 (a) and MIX2 (b) the temperature development in the cylindrical specimen exposed to high temperature. The temperature of the furnace is indicated with a

dashed line, while solid lines represent the temperature history on the surface and in the centre of the cylinder in both experimental and numerical case. Figs. 10a-b show the temperature differences between the surface and the centre of the specimens measured during the tests and the corresponding numerical results. The accordance between numerical and experimental results is quite good, especially in the case of MIX2. For MIX1, in fact, the first part of heating shows a strange behaviour with temperature difference between core and surface practically zero for more than one hour.

Fig. 11 provides information about damaging of the specimen during heating. Specifically, it shows the history of total damage in three different points (on the surface, in the centre and in the middle of the radius) compared with temperature difference developments. Corresponding to the maximum value of ΔT, a sharp increase of mechanical damage parameter d (with a maximum value equal to 80%) may be observed for both of the mixtures considered in the simulation.

Fig. 12a shows developments (2.5 cm from the surface of the specimen) of the gas pressure, and Fig. 12b the thermo-chemical damage, for MIX1 and MIX2. It is worth

Table3 - Initial conditions used in the numerical simulation		
Variable	**Unit**	**Value**
Gas pressure	[Pa]	101325
Relative humidity	[-]	0.5
Temperature	[K]	298.15

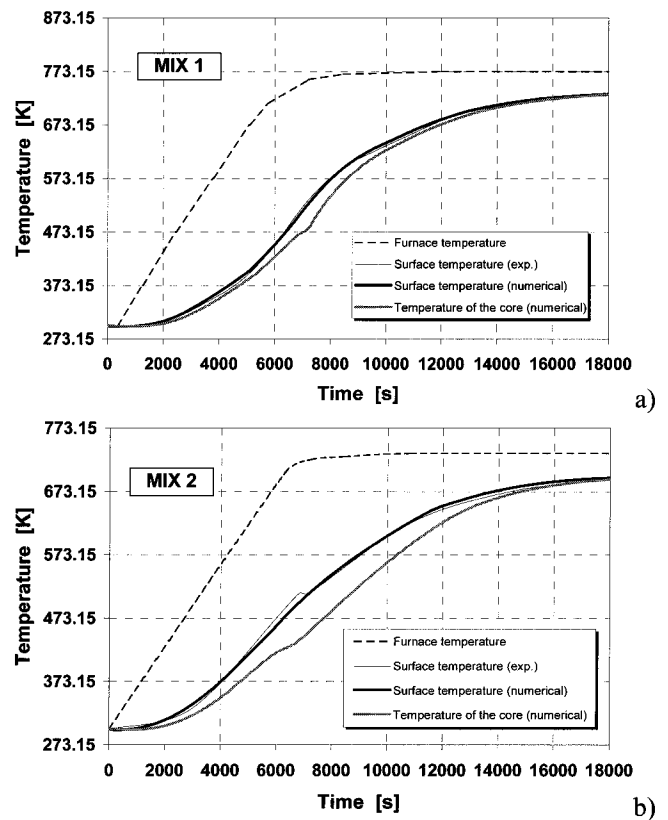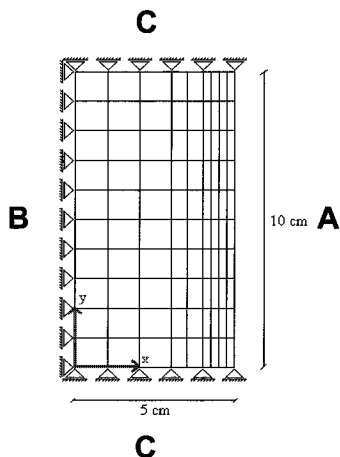| Table 4 - Boundary conditions used in the numerical simulation		
Side	**Variables**	**Values and coefficients**
A	u_x	$u_x = 0$
	u_y	$u_y = 0$
	p^g	$p^g = 101325$ [Pa]
	p^c	$p^{gw} = 1000$ [Pa], $\beta_c =$ variable
	T: convective	$T =$ ISO-Fire [K], $\alpha_c =$ variable
	T: radiative	$e\sigma_0 = 5.1 \cdot 10^{-8}$ [W m^{-2}K^{-1}]
B	u_x	$U_x = 0$
	p^g	$q^g = 0$
	p^c	$q^{gw} = q^w = 0$
	T	$q^T = 0$
C	u_y	$u_y = 0$
	p^g	$q^g = 0$
	p^c	$q^{gw} = q^w = 0$
	T	$q^T = 0$

C

B   10 cm   A

5 cm

C

Fig. 9 - Temperature development (numerical and experimental) on the surface of the specimen and in the core of the cylinders: a) MIX1, b) MIX2.
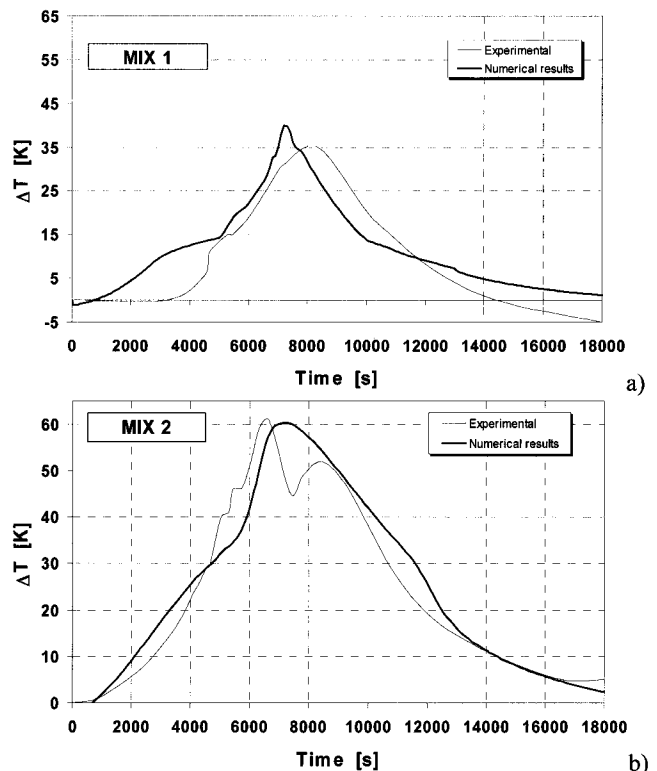

Fig. 10 - Temperature difference (numerical and experimental) between the surface of the specimen and the centre of cylinder: a) MIX1, b) MIX2.

to note the considerably different behaviour of the two concretes in terms of maximum value of p^g and value of V
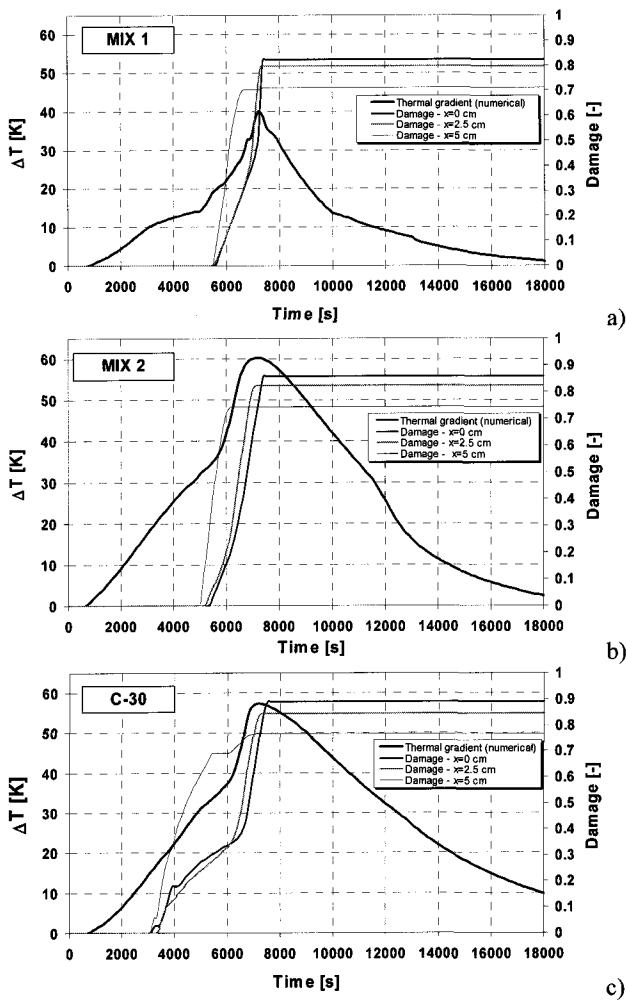
229

Fig. 11 - Time history of temperature difference (between the surface of the specimen and the core of the cylinders) and of total damage: a) MIX1, b) MIX2, c) C-30. X is the distance from the axis of the cylinder.
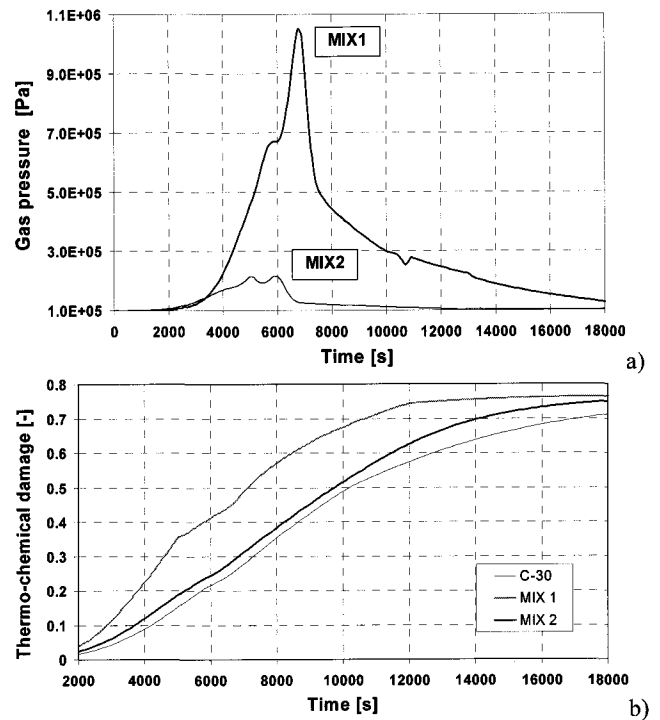

Fig. 12 - Gas pressure (a) and thermo-chemical damage (b) changes in time for MIX1 and MIX2 at 2.5 cm from the surface of the specimen.
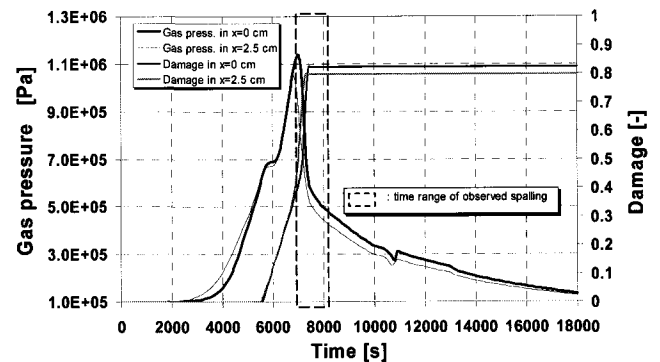

Fig. 13 - Gas pressure and mechanical damage changes in time for MIX1 on the surface and at 2.5 cm from the surface of the specimen.

reached during heating process. Similarly to the increase of mechanical damage, the peak of gas pressure corresponds to the maximum value of temperature differences ΔT.

The time range between 7200 s and 8000 s seems to be the critical range during which the material achieves a state favourable to spalling occurrence. Indeed, in the case of MIX1, the specimen experienced explosive spalling right in this range of time, while the specimen made with the concrete type 2 did not show this phenomenon. The explanation of this different behaviour of the two materials could be their different microstructure and loss of strength properties due to cracking and thermo-chemical deterioration, resulting from different water/cement ratio (see Table 2), which lead to pressure development characterised by completely different absolute values.

This critical time range is evidenced in Fig. 13 and it corresponds well to the time range of observed explosive spalling in NIST laboratories for concrete MIX1.

Furthermore, reconstruction of the exploded specimens carried out by NIST researchers by means of rendering techniques, showed that, in all cases, a core, which measured approximately 70 mm at maximum width, was the largest remaining piece of concrete. This core is surrounded by an approximately 20mm thick concrete outer

shell. The depth of 20mm appears to be the location of the primary fracture surface. The numerical results show a similar behaviour. Fig. 14a) shows the reconstructed specimen with the external layer 20mm thick, while Fig. 14b) shows the damage distribution along the thickness of the specimen (i.e. in radial direction) at different time stations. It is possible to observe that at time corresponding to explosive spalling (solid line) a layer 2cm thick has reached the maximum value of damage.

The presented results of numerical simulations, show that both pore pressure and thermally induced strains can be identified as responsible for the spalling occurrence, and that they play a primary or secondary role depending on the particular conditions prevailing. For the analysed HPC concretes, the MIX 1 specimens, having lower value of the w/c ratio, spalled explosively mainly due to the high gas pressure value and relatively high level of thermo-chemical deterioration, even if the temperature gradients were 50%
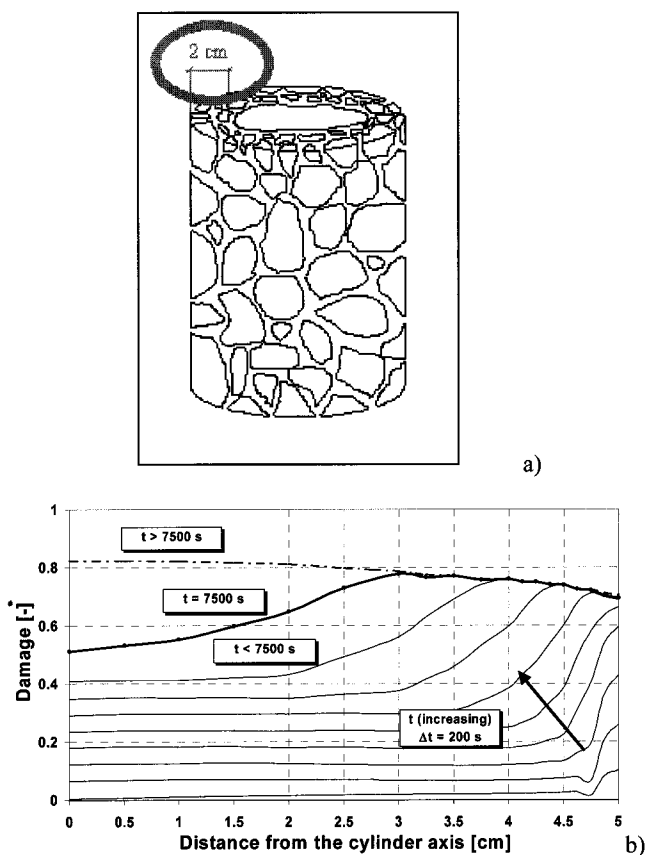
Fig. 14 - a) Rendering of the fracture formation, b) Total damage distribution in radial direction for MIX1: dashed line represents the final situation (specimen exploded), the solid line represents the situation at the time when first spalling occurred.
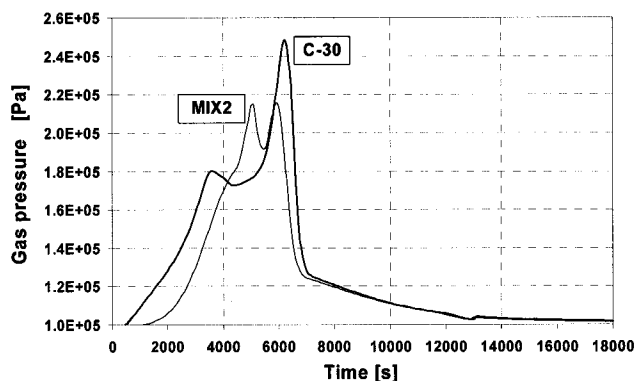

Fig. 15 - Gas pressure changes in time for C-30 and MIX2 at 2.5 cm from the surface of the specimen.

lower than in the MIX 2. During the NIST tests the all three specimens done of the MIX 1 experienced explosive spalling, confirming the importance of gas pressure as a reason of the phenomenon. On the other hand, one of the three MIX 2 cylinders experienced spalling, despite of much lower pressure value (about 5 times) and lover thermo-chemical induced deterioration (about 30%), but about 50% greater temperature gradients. This shows that also thermally induced strains can be a dominant reason of explosive spalling, even if its occurrence seems to be less likely.

To analyse differences between performance of heated NSC and HPC, numerical simulation of the same NIST test, but for the C-30 concrete (see Table 1), has been performed. No tests for this type of concrete are reported in [4, 5, 12, 16], hence results of these simulation cannot be compared to the experimental ones. Fig. 11c shows history of mechanical damage (at three different distances from the cylinder axis) and the difference of temperature between the surface and the core of the cylinder. Development of thermo-chemical deterioration of the C-30 concrete is compared in Fig. 12 with those of the MIX 1 and MIX 2. Temporal developments of the gas pressure, for the C-30 and MIX 2, 2.5 cm from the surface of the specimen, are compared in Fig. 15. The performance of the C-30 concrete is somewhat similar to the MIX 2, but the vapour pressure starts increasing earlier in this concrete due to the higher content of chemically bound water (higher w/c ratio), and it reaches higher maximal value (about 0.4 MPa) as compared to the MIX 2. Then, mechanical damaging of this concrete starts after 52 minutes, *i.e.* about 30 minutes earlier than in the MIX 2 (about 40 minutes earlier than in the MIX 1). In the time span, when the temperature gradient reaches its maximum values, the mechanical damage increases in a slightly slower way (~2.3%/min) than in the MIX 2 (~3%/min), and the level of thermo-chemically induced deterioration of concrete is similar as in MIX 2. Concluding, one can expect a similar likelihood of explosive spalling of the C-30 concrete as for the MIX 2, because in the analysed temperature range both materials are exposed to similar pressures, and thermo-chemical and mechanical damage, describing advancement of deterioration of the material strength properties.

6. CONCLUSIONS

An analysis of deformations of concrete, in particular High Performance Concrete, exposed to high temperature has been presented. It is based on physical interpretation of experimental results in the framework of a mechanistic approach, distinguishing between free thermal strains, shrinkage strains and thermo-chemical strains which is unusual in the literature. Shrinkage strains are determined using thermodynamic relationships via capillary pressure and area fraction coefficients, while thermo-chemical strains are related to thermo-chemical damage. Moreover, a classical thermal creep formulation has been modified and introduced in a fully coupled model of thermal, hygral, chemical and stress phenomena in concrete at high temperature taking into account most of the important features of the material behaviour at these conditions. It allows for realistic risk assessment of thermal spalling, considering both effects of pore pressure build-up and the accumulated strain energy, together with thermo-chemical material degradation and cracking. The results of numerical simulations are in good accordance with experimental tests.

ACKNOWLEDGMENTS

APPENDIX

Below we explore the second law of Thermodynamics, applied for the multi-phase porous medium, which skeleton experiences chemical reactions (dehydration) and material deterioration (thermo-chemical and mechanical damage). This allows us to define several important quantities used in our model (*e.g.* capillary pressure, net effective stress tensor of the solid phase) and obtain some thermodynamic restrictions imposed on the evolution equations for the skeleton dehydration and deterioration processes. For the sake of brevity, we present here only the main steps of the whole procedure and "abbreviated" form of the equations (but containing all terms used in further developments), which are presented in detail in [30] for the finite deformations of the solid skeleton and in [21] for another form of the Helmholtz free energy. All symbols are explained in the Nomenclature. For convenience of the reader we have kept the original symbols for the Bishop effective stress and "net" effective stress tensors which were used in [30].

The starting point for further developments is the second law of Thermodynamics written for a multiphase system. It states that for any process, the rate of net entropy production must be non-negative:

$$\Lambda = \Lambda^s + \Lambda^w + \Lambda^g + \sum_{\alpha\beta=gs,gw,sw} \Lambda^{\alpha\beta} \geq 0. \qquad (A1)$$

After expressing the terms for the rate of net production of entropy in the individual phases and interfaces, Equation (A1) has the following form [30]:

$$(1-n)\rho^s \frac{D^s \lambda^s}{Dt} - div\left((1-n)\frac{\mathbf{q}^s}{T^s}\right) +$$

$$-(1-n)\rho^s \frac{h^s}{T^s} - \hat{\Phi}^s_{sg} - \hat{\Phi}^s_{sw} + n S_w \rho^w \frac{D^w \lambda^w}{Dt} +$$

$$-div\left(n S_w \frac{\mathbf{q}^w}{T^w}\right) - n S_w \rho^w \frac{h^w}{T^w} - \hat{\Phi}^w_{wg} - \hat{\Phi}^w_{ws} +$$

$$n S_g \rho^g \frac{D^g \lambda^g}{Dt} - div\left(n S_g \frac{\mathbf{q}^g}{T^g}\right) + - n S_g \rho^g \frac{h^g}{T^g} - \hat{\Phi}^g_{gw} +$$

$$-\hat{\Phi}^g_{gs} + \sum_{\alpha\beta=gs,gw,sw}\left[a^{\alpha\beta}\Gamma^{\alpha\beta}\frac{D^{\alpha\beta}\lambda^{\alpha\beta}}{Dt} + \right.$$

$$-div\left(a^{\alpha\beta}\frac{\mathbf{q}^{\alpha\beta}}{T^{\alpha\beta}}\right) - a^{\alpha\beta}\Gamma^{\alpha\beta}\frac{h^{\alpha\beta}}{T^{\alpha\beta}} +$$

$$\left(\hat{\Phi}^\alpha_{\alpha\beta} + \hat{e}^\alpha_{\alpha\beta}\lambda^{\alpha,\alpha\beta}\right) + \left(\hat{\Phi}^\beta_{\alpha\beta} + \hat{e}^\beta_{\alpha\beta}\lambda^{\beta,\alpha\beta}\right) - \hat{\Phi}^{\alpha\beta}_{wgs}\left.\right] \geq 0.$$
$$(A2)$$

In further developments it is convenient to use the Helmholtz free energy, defined for the bulk phases as

$$A^\alpha = E^\alpha - T^\alpha \lambda^\alpha, \quad \alpha = s, w, g, \qquad (A3)$$

and the interfaces as

$$A^{\alpha\beta} = E^{\alpha\beta} - T^{\alpha\beta}\lambda^{\alpha\beta}, \quad \alpha\beta = gw, ws, gs. \qquad (A4)$$

Introduction of the energy balance equation allows the rate of net production of entropy in the solid phase to be expressed as, see [30]:

$$\Lambda^s = -\frac{(1-n)\rho^s}{T^s}\left[\frac{D^s A^s}{Dt} + \lambda^s \frac{D^s T^s}{Dt}\right] +$$

$$+\frac{(1-n)}{\left(T^s\right)^2}\mathbf{q}^s \cdot grad\, T^s + \qquad (A5)$$

$$+\frac{1-n}{T^s}\sigma^s : grad\, \mathbf{v}^s - \hat{\Phi}^s_{sg} - \hat{\Phi}^s_{sw} + \frac{\hat{Q}^s_{sw}}{T^s} + \frac{\hat{Q}^s_{sg}}{T^s}.$$

After similar transformations carried out for all the other phases and for the three interfaces, and after application of (A3) and (A4), the entropy inequality (A1) can be written as:

$$-\frac{(1-n)\rho^s}{T^s}\left(\frac{D^s A^s}{Dt} + \lambda^s \frac{D^s T^s}{Dt}\right) +$$

$$-\frac{n S_w \rho^w}{T^w}\left(\frac{D^w A^w}{Dt} + \lambda^w \frac{D^w T^w}{Dt}\right) +$$

$$-\frac{n S_g \rho^g}{T^g}\left(\frac{D^g A^g}{Dt} + \lambda^g \frac{D^g T^g}{Dt}\right) +$$

$$+\frac{1-n}{\left(T^s\right)^2}\mathbf{q}^s \cdot grad\, T^s + \frac{n S_w}{\left(T^w\right)^2}\mathbf{q}^w \cdot grad\, T^w +$$

$$+\frac{n S_g}{\left(T^g\right)^2}\mathbf{q}^g \cdot grad\, T^g + \frac{1-n}{T^s}\sigma^s : \mathbf{d}^s + \frac{n S_w}{T^w}\sigma^w : \mathbf{d}^w +$$

$$+\frac{n S_g}{T^g}\sigma^g : \mathbf{d}^g + \sum_{\alpha\beta=sg,sw,gw}\frac{a^{\alpha\beta}\mathbf{s}^{\alpha\beta}}{T^{\alpha\beta}} : \mathbf{d}^{\alpha\beta} +$$

$$-\sum_{\alpha\beta=sg,sw,gw}\frac{a^{\alpha\beta}\Gamma^{\alpha\beta}}{T^{\alpha\beta}}\left(\frac{D^{\alpha\beta}A^{\alpha\beta}}{Dt} + \lambda^{\alpha\beta}\frac{D^{\alpha\beta}T^{\alpha\beta}}{Dt}\right) +$$

$$\sum_{\alpha\beta=sg,sw,gw}\frac{a^{\alpha\beta}}{\left(T^{\alpha\beta}\right)^2}\mathbf{q}^{\alpha\beta} \cdot \nabla T^{\alpha\beta} +$$

$$+ [\ TERMS\ RELATED\ TO\ BODY\ SUPPLIES\ ] \geq 0$$
$$(A6)$$

In this equation we have introduced the strain rate tensors for bulk phases $\mathbf{d}^\alpha$ ($\alpha = s, w, g$) and for interfaces $\mathbf{d}^{\alpha\beta}$ ($\alpha\beta = gw, gs, ws$). Because of symmetry of the partial stress tensor σ^α and the surface stress tensor $\mathbf{s}^{\alpha\beta}$, the following identities hold:

$$\sigma^\alpha : grad\, \mathbf{v}^\alpha = \sigma^\alpha : \mathbf{d}^\alpha, \qquad (A7)$$

$$\mathbf{s}^{\alpha\beta} : grad\, \mathbf{w}^{\alpha\beta} = \mathbf{s}^{\alpha\beta} : \mathbf{d}^{\alpha\beta}. \qquad (A8)$$

The Helmholtz free energy for the bulk phases is assumed to have the following functional forms:

$$A^w = A^w\left(\rho^w, T^w, S_w\right), \qquad A^g = A^g\left(\rho^g, T^g, S_g\right),$$

$$A^s = A^s\left(\rho^s, T^s, \varepsilon^s, S_w, \Gamma_{dehydr}, D\right),$$

$$\tag{A9}$$

and for the interfaces:

$$A^{\alpha\beta} = A^{\alpha\beta}\left(\Gamma^{\alpha\beta}, T^{\alpha\beta}, a^{\alpha\beta}, S_w\right), \qquad \alpha\beta = gw, ws, gs \tag{A10}$$

One must underline, that in Equation (A9) for the solid skeleton, effect of the two internal variables, Γ_{dehydr} and D, has been additionally considered, as compared to [30]. After calculating the material time derivatives of the Helmholtz free energies (A9)-(A10), the entropy inequality becomes:

$$-\frac{(1-n)\rho^s}{T^s}\frac{D^s T^s}{Dt}\left(\frac{\partial A^s}{\partial T^s}+\lambda^s\right)+$$

$$-\frac{nS_w\rho^w}{T^w}\frac{D^w T^w}{Dt}\left(\frac{\partial A^w}{\partial T^w}+\lambda^w\right)+$$

$$-\frac{nS_g\rho^g}{T^g}\frac{D^g T^g}{Dt}\left(\frac{\partial A^g}{\partial T^g}+\lambda^g\right)+$$

$$-\sum_{\alpha\beta=sg,sw,gw}\frac{a^{\alpha\beta}\Gamma^{\alpha\beta}}{T^{\alpha\beta}}\frac{D^{\alpha\beta}T^{\alpha\beta}}{Dt}\left(\frac{\partial A^{\alpha\beta}}{\partial T^{\alpha\beta}}+\lambda^{\alpha\beta}\right)+$$

$$+\frac{nS_w}{T^w}\left(p^w\mathbf{I}+\boldsymbol{\sigma}^w\right):\mathbf{d}^w+\frac{nS_g}{T^g}\left(p^g\mathbf{I}+\boldsymbol{\sigma}^g\right):\mathbf{d}^g+$$

$$+\frac{1-n}{T^s}\left(p^s\mathbf{I}+\boldsymbol{\sigma}^s\right):\mathbf{d}^s-\left[\frac{(1-n)\rho^s}{T^s}\frac{\partial A^s}{\partial\varepsilon^s}\right]:\mathbf{d}^s+$$

$$+\frac{D^s n}{Dt}\left(\frac{S_w p^w}{T^w}+\frac{S_g p^g}{T^g}-\frac{p^s}{T^s}\right)+$$

$$+\frac{(1-n)}{T^s}A_\Gamma\frac{D^s\Gamma_{dehydr}}{Dt}+\frac{(1-n)}{T^s}Y\frac{D^s D}{Dt}+$$

$$+\frac{D^s S_w}{Dt}\begin{pmatrix}\dfrac{np^w}{T^w}-\dfrac{np^g}{T^g}-\dfrac{nS_w\rho^w}{T^w}\dfrac{\partial A^w}{\partial S_w}+\\[2mm]\dfrac{nS_g\rho^g}{T^g}\dfrac{\partial A^g}{\partial S^g}-\dfrac{(1-n)\rho^s}{T^s}\dfrac{\partial A^s}{\partial S_w}\\[2mm]-\displaystyle\sum_{\alpha\beta=sg,sw,gw}\dfrac{a^{\alpha\beta}\Gamma^{\alpha\beta}}{T^{\alpha\beta}}\dfrac{\partial A^{\alpha\beta}}{\partial S_w}\end{pmatrix}+$$

$$+\begin{bmatrix}TERMS\ RELATED\ TO\ BODY\ SUPPLIES,\\ DEFORMATION\ OF\ THE\ INTERFACES,\\ PHASE\ CHANGES\ AND\ HEAT\ FLUXES\end{bmatrix}\geq 0 \tag{A11}$$

The following definitions have been introduced into (A11):

- macroscopic pressure of the α phase,

$$p^\alpha = \left(\rho^\alpha\right)^2\frac{\partial A^\alpha}{\partial\rho^\alpha}, \qquad (\alpha = s, w, g), \tag{A12}$$

- macroscopic interfacial tension of the $\alpha\beta$ interface,

$$\gamma^{\alpha\beta} = -\left(\Gamma^{\alpha\beta}\right)^2\frac{\partial A^{\alpha\beta}}{\partial\Gamma^{\alpha\beta}}, \qquad (\alpha\beta = sw, wg, gs), \tag{A13}$$

- chemical affinity, being the driving force of the chemical reaction, correlated to the rate of the dehydration extent, $\dot{\Gamma}_{dehydr} = \dfrac{D^s\Gamma_{dehydr}}{Dt}$, by means of an evolution law of the Arrhenius-type,

$$A_\Gamma = -\frac{\partial A^s}{\partial\Gamma_{dehydr}}\rho^s \tag{A14}$$

together with identities:

$$div\,\mathbf{v}^\alpha = \mathbf{d}^\alpha:\mathbf{I}, \qquad (\alpha = s, w, g) \tag{A15}$$

$$T^{\alpha,s} = T^\alpha - T^s \tag{A16}$$

In the l.h.s. of inequality (A11) appear quantities in brackets multiplied by: $\dfrac{D^\alpha T^\alpha}{Dt}$, $\dfrac{D^{\alpha\beta}T^{\alpha\beta}}{Dt}$, $\mathbf{d}^\alpha, \mathbf{d}^{\alpha\beta}$ which are not primary variables. Therefore, the coefficient of these variables must be always zero, because (A11) is valid for all thermodynamic states. Hence the following relationships for the specific entropies and stress tensors are obtained:

$$\lambda^\alpha = -\frac{\partial A^\alpha}{\partial T^\alpha}, \quad (\alpha = w, g, s) \qquad \lambda^{\alpha\beta} = -\frac{\partial A^{\alpha\beta}}{\partial T^{\alpha\beta}},$$

$$(\alpha\beta = gw, ws, gs), \tag{A17}$$

$$\mathbf{s}^{\alpha\beta} = \gamma^{\alpha\beta}\mathbf{I}, \qquad \boldsymbol{\sigma}^w = -p^w\mathbf{I}, \qquad \boldsymbol{\sigma}^g = -p^g\mathbf{I}. \tag{A18}$$

In particular, the total (nominal) stress tensor of the solid phase is defined by:

$$\boldsymbol{\sigma}^s = \boldsymbol{\sigma}_e^s - p^s\mathbf{I}, \tag{A19}$$

where:

$$\boldsymbol{\sigma}_e^s = \rho^s\frac{\partial A^s}{\partial\varepsilon^s} \tag{A20}$$

is the effective stress tensor of the solid phase,

$$p^s\left(\rho^s, T^s, \varepsilon^s, S^w\right) = \left(\rho^s\right)^2\frac{\partial A^s}{\partial\rho^s} \tag{A21}$$

is the thermodynamic pressure of the solid phase,

$$Y = -\rho^s\frac{\partial A^s}{\partial D} \tag{A22}$$

is the damage energy release rate,

$$p^c = \frac{T^{wg}}{n}\begin{bmatrix}-\dfrac{nS_w\rho^w}{T^w}\dfrac{\partial A^w}{\partial S_w}+\dfrac{nS_g\rho^g}{T^g}\dfrac{\partial A^g}{\partial S_g}\\[2mm]-\dfrac{(1-n)\rho^s}{T^s}\dfrac{\partial A^s}{\partial S_w}-\\[2mm]\displaystyle\sum_{\alpha\beta=sg,sw,gw}\dfrac{a^{\alpha\beta}\Gamma^{\alpha\beta}}{T^{\alpha\beta}}\dfrac{\partial A^{\alpha\beta}}{\partial S^w}\end{bmatrix}, \tag{A23}$$

is the macroscopic "thermodynamic" capillary pressure.

We introduce damage into the elastic constitutive law in a classical manner, considering that only the elastic properties of the material are affected by damage parameter D (containing both the mechanical and thermo-chemical components) and that the dependence on damage is due to the stiffness matrix:

$$\Lambda = \Lambda(D), \quad \sigma_e^s = \Lambda(D) : \varepsilon^s . \qquad (A24)$$

Hence, Y is a quadratic form, positively defined, since $\dfrac{\partial \Lambda(D)}{\partial D} < 0$, i.e. the stiffness decreases for increasing damage.

In fact, considering the second derivative of the Helmholtz free energy and exploiting the Maxwell symmetries, we have:

$$\frac{\partial^2 A^s}{\partial D \partial \varepsilon^s} = \frac{\partial \Lambda(D)}{\partial D} : \varepsilon^s = \frac{\partial^2 A^s}{\partial \varepsilon^s \partial D} = -\frac{\partial Y}{\partial \varepsilon^s} \qquad (A25)$$

and integrating the latter expression with respect to ε^s we obtain a quadratic form for Y:

$$Y = -\frac{1}{2} \frac{\partial \Lambda(D)}{\partial D} : \varepsilon^s : \varepsilon^s + C , \qquad (A26)$$

where C is a constant independent on damage ($C=0$, since $Y=0$ for $D=0$).

Thus the sufficient condition to satisfy entropy inequality is $\dot{D} = \dfrac{D^s D}{Dt} \geq 0$.

In our model we adopt the Mazars theory of damage, i.e. the material is supposed to behave elastically and to remain isotropic. Application of the true stress concept, [38],

$$\sigma_e^s = (1 - D)\tilde{\sigma}_e^s , \qquad (A27)$$

where $\tilde{\sigma}_e^s$ is the "net effective stress" (in the sense of damage mechanics and porous media), leads to the following form of the constitutive relationship for the solid phase:

$$\tilde{\sigma}_e^s = \Lambda_0 : \varepsilon^s = \Lambda_0 : \left(\varepsilon_{tot} - \varepsilon_{th} - \varepsilon_{tr} - \varepsilon_{tchem} \right) \qquad (A28)$$

where Λ_0 is the initial stiffness tensor and $\varepsilon_{tot}, \varepsilon_{th}, \varepsilon_{tr}, \varepsilon_{tchem}$ are the total-, thermal-, thermal creep- and thermo-chemical strain tensors, respectively.

Taking into account (A19) and (A27), the "net" effective stress tensor is equal to:

$$\tilde{\sigma}_e^s = \frac{\sigma^s + p^s \mathbf{I}}{(1 - D)} = \frac{\sigma^s + p^s \mathbf{I}}{(1 - d)(1 - V)} , \qquad (A29)$$

where p^s is given by (3).

A similar equation was applied by Bourgeois et al. [39] for modelling of elasto-plastic damage due to drying shrinkage of concrete, based on the theory by Coussy [40].

NOMENCLATURE

A^α specific Helmholtz free energy for the bulk phase α [J kg^{-1}]

$A^{\alpha\beta}$ specific Helmholtz free energy for the interface $\alpha\beta$ [J kg^{-1}]

$a^{\alpha\beta}$ specific surface of the $\alpha\beta$-interface [m^{-1}]

C_p effective specific heat of porous medium [J kg^{-1} K^{-1}]

C_p^g specific heat of gas mixture [J kg^{-1} K^{-1}]

C_p^w specific heat of liquid phase [J kg^{-1} K^{-1}]

D total damage parameter [-]

d mechanical damage parameter [-]

$\mathbf{d}^s$ strain rate tensor [s^{-1}]

$\mathbf{D}_d^{gw}$ effective diffusivity tensor of water vapour in dry air [m^2 s^{-1}]

E   Young's modulus [Pa]

e emissivity of the interface [-]

$\hat{e}$ exchange term [kg m^{-3} s^{-1}]

E_0 Young's modulus of mechanically undamaged material [Pa]

E^α internal energy of bulk phase α [J kg^{-1}]

$E^{\alpha\beta}$ internal energy of interface $\alpha\beta$ [J kg^{-1}]

f_c compressive strength of concrete [MPa]

f_t tensile strength of concrete [MPa]

$\mathbf{g}$ gravity acceleration [m s^{-2}]

h^α heat source in the bulk phase α [W kg^{-1}]

$h^{\alpha\beta}$ heat source on the interface $\alpha\beta$ [W kg^{-1}]

$\mathbf{I}$ unit tensor [-]

$\mathbf{J}_d^{gw}$ diffusive flux of vapour [kg m^{-2} s^{-1}]

$\mathbf{J}_d^{ga}$ diffusive flux of dry air [kg m^{-2} s^{-1}]

K_T modified bulk modulus of the whole porous medium [Pa]

K_s modified bulk modulus of the grain material [Pa]

$\mathbf{k}$ absolute permeability tensor [m^2]

k absolute permeability (scalar) [m^2]

$k^{r\pi}$ relative permeability of π-phase (π=g,w) [-]

$\dot{m}_{dehydr}$ rate of mass due to dehydration [kg m^{-3} s^{-1}]

$\dot{m}_{vap}$ rate of mass due to phase change [kg m^{-3} s^{-1}]

n total porosity (pore volume/total volume) [-]

p_{atm} atmospheric pressure [Pa]

p^c capillary pressure [Pa]

p^g pressure of gas phase [Pa]

p_o^g initial value of gas pressure [Pa]

p^w pressure of liquid water [Pa]

p^s solid skeleton pressure [Pa]

p^{ga} dry air partial pressure [Pa]

p^{gw} water vapour partial pressure [Pa]

$\mathbf{q}^\alpha$ heat flux vector for the bulk phase α [W m^{-2}]

$\mathbf{q}^{\alpha\beta}$ heat flux vector for the interface $\alpha\beta$ [W m^{-2}]

$\tilde{\mathbf{q}}$ heat flux vector [W m^{-2}]

$\hat{Q}$ body supply of heat [W m^{-2}]

R   gas constant (8314.41 J kmol^{-1} K^{-1})

RH   relative humidity [-]

S_w liquid phase volumetric saturation (liquid volume/pore volume) [-]

S total area [m^2]

$\tilde{S}$ resistant area of damaged material [m^2]

T absolute temperature [K]

T_{cr} critical temperature of water [K]

T_{max} maximum temperature attained during dehydration process [K]

t time [s]

$\mathbf{u}$	displacement vector of solid matrix [m]
V	thermo-chemical damage parameter [-]
$\mathbf{v}^{gs}$	relative velocity of gaseous phase [m s^{-1}]
$\mathbf{v}^{ws}$	relative velocity of liquid phase [m s^{-1}]
x_s^{ws}	solid surface fraction in contact with the wetting water film [-]

Greek symbols

α	generic bulk phase
α	Biot's constant [-]
α_c	convective heat transfer coefficient [W m^{-2} K^{-1}]
$\alpha\beta$	generic interface of α- and β-phases
β_{tchem}	thermo-chemical strain coefficient [K^{-1}]
β_c	convective mass transfer coefficient [m s^{-1}]
β_s	cubic thermal expansion coefficient of solid [K^{-1}]
β_{swg}	combine (solid + liquid + gas) cubic thermal expansion coefficient [K^{-1}]
β_{sw}	combine (solid + liquid) cubic thermal expansion coefficient [K^{-1}]
$\bar{\beta}_{tr}$	normalised transient thermal strain coefficient [K^{-1} s]
β_w	thermal expansion coefficient of liquid water [K^{-1}]
ΔH_{vap}	enthalpy of vaporization per unit mass [J kg^{-1}]
ΔH_{dehydr}	enthalpy of dehydration per unit mass [J kg^{-1}]
Δt	time step [s]
ε_{el}	elastic strain tensor [-]
ε_{sh}	shrinkage strain tensor [-]
ε_{tchem}	thermo-chemical strain tensor [-]
ε_{th}	thermal strain tensor [-]
ε_{tot}	total strain tensor [-]
ε_{tr}	transient thermal strain tensor [-]
$\bar{\varepsilon}_{tr}$	normalized transient thermal strain [-]
$\tilde{\varepsilon}$	equivalent strain in damage theory of Mazars [-]
$\Gamma^{\alpha\beta}$	surface excess mass density of $\alpha\beta$-interface [kg m^{-2}]
Γ_{dehydr}	degree of dehydration [-]
$\gamma^{\alpha\beta}$	macroscopic interfacial tension of the $\alpha\beta$-interface [J m^{-2}]
μ^{π}	dynamic viscosity of the constituent π-phase (π=g,w) [μPa s]
λ	specific entropy [J kg^{-1} K^{-1}]
Λ	rate of net production of entropy [W kg^{-1} K^{-1}]
Λ	stiffness matrix of damaged material [Pa]
Λ_o	stiffness matrix of undamaged material [Pa]
χ_{eff}	effective thermal conductivity [W m^{-1} K^{-1}]
Π^w	disjoining pressure [Pa]
ρ	apparent density of porous medium [kg m^{-3}]
ρ^g	gas phase density [kg m^{-3}]
ρ^w	liquid phase density [kg m^{-3}]
ρ^s	solid phase density [kg m^{-3}]
ρ^{ga}	mass concentration of dry air in gas phase [kg m^{-3}]
ρ^{gw}	mass concentration of water vapour in gas phase [kg m^{-3}]
$\hat{\Phi}$	body entropy supply [W kg^{-1} K^{-1}]
σ	Cauchy stress tensor [Pa]
σ_e^s, σ''	Bishop effective stress tensor [Pa]
$\bar{\sigma}_e^s, \bar{\sigma}$	"net" effective stress tensor [Pa]
σ_o	Stefan-Boltzmann constant [5.670 $\times$ 10^{-8} W m^{-2} K^{-1}]
Ψ	Jacobian matrix

Operators and averaged values

$\dfrac{\partial}{\partial t}$	partial time derivative
grad	gradient operator (spatial description)

div   divergence operator (spatial description)

REFERENCES

[1] Bažant, Z.P. and Thonguthai, W., 'Pore pressure and drying of concrete at high temperature', *J. Engng. Mech. ASCE* **104** (1978) 1059-1079.

[2] England, G.L. and Khoylou, N., 'Moisture flow in concrete under steady state non-uniform temperature states: experimental observations and theoretical modelling', *Nucl. Eng. Des.* **156** (1995) 83-107.

[3] Bažant, Z.P. and Kaplan, M.F., 'Concrete at High Temperatures: Material Properties and Mathematical Models', (Longman, Harlow, 1996).

[4] Phan, L.T., 'Fire performance of high-strength concrete: a report of the state-of-the-art', Res. Report NISTIR 5934, pp.105, National Institute of Standards and Technology, Gaithersburg, 1996.

[5] Phan, L.T., Carino, N.J., Duthinh, D. and Garboczi, E. (eds.), Proc. Int. Workshop on Fire Performance of High-Strength Concrete, Gaithersburg (MD), USA, February 13-14, 1997, NIST Special Publication 919, NIST, 1997.

[6] Brite Euram III BRPR-CT95-0065 HITECO, Understanding and industrial application of High Performance Concrete in High Temperature Environment – Final Report, 1999.

[7] Ulm, F.-J., Acker, P. and Levy, M., 'The "Chunnel" fire. II. Analysis of concrete damage', *J. Eng. Mech. ASCE* **125**(3) (1999) 283-289.

[8] Ulm, F.-J., Coussy, O. and Bažant, Z., 'The "Chunnel" fire. I. Chemoplastic softening in rapidly heated concrete', *J. Eng. Mech., ASCE* **125**(3) (1999) 272-282.

[9] Gawin, D., Majorana, C.E. and Schrefler, B.A., 'Numerical analysis of hygro-thermic behaviour and damage of concrete at high temperature', *Mech. Cohes.-Frict. Mater.* **4** (1999) 37-74.

[10] Bentz, D.P., 'Fibers, percolation, and spalling of high-performance concrete', *ACI Materials Journal* **97**(3) (2000) 351-359.

[11] Nechnech, W., Reynouard, J.M. and Meftah, F., 'On modelling of thermo-mechanical concrete for the finite element analysis of structures submitted to elevated temperatures', in: Proc. Fracture Mechanics of Concrete Structures, R. de Borst, J. Mazars, G. Pijaudier-Cabot, J.G.M. van Mier, Eds (Swets & Zeitlinger, Lisse, 2001) 271-278.

[12] Phan, L.T., Lawson, J.R. and Davis, F.L., 'Effects of elevated temperature exposure on heating characteristics, spalling, and residual properties of high performance concrete', *Mater. Struct.* **34** (March 2001) 83-91.

[13] Sullivan, P.J.E., 'Deterioration and spalling of high strength concrete under fire', Offshore Technology Report 2001/074, HSE Books, Sudbury, 2001, pp.77.

[14] Gawin, D., Pesavento, F. and Schrefler, B.A., 'Simulation of damage – Permeability coupling in hygro-thermo-mechanical analysis of concrete at high temperature', *Commun. Numer. Meth. Engrg.* **18** (2002) 113-119.

[15] Gawin, D., Pesavento, F. and Schrefler, B.A., 'Modelling of hygro-thermal behaviour and damage of concrete at temperature above the critical point of water', *Int. J. Numer. Anal. Meth. Geomech.* **26** (2002) 537-562.

[16] Phan, L.T. and Carino, N.J., 'Effects of test conditions and mixture proportions on behavior of high-strength concrete exposed to high temperature', *ACI Materials Journal* **99**(1) (2002) 54-66.

[17] Gawin, D., Pesavento, F. and Schrefler, B.A., 'Modelling of hygro-thermal behaviour of concrete at high temperature with thermo-chemical and mechanical material degradation', *Comput. Methods Appl. Mech. Engrg.* **192** (2003) 1731-1771.

[18] Khoury, G.A., 'Strain components of nuclear-reactor-type concretes during first heating cycle', *Nuclear Engineering and Design* **156** (1995) 313-321.

[19] Baroghel-Bouny, V., Mainguy, M., Lassabatère, T. and Coussy O., 'Characterization and identification of equilibrium and transfer moisture properties for ordinary and high-performance cementitious materials', *Cem. Concr. Res.* **29** (1999) 1225-1238.

[20] Schrefler, B.A. and Gawin, D., 'The effective stress principle: incremental or finite form?', *Int. J. Numer. Anal. Meth. Geomech.* **20** (1996) 785-815.

[21] Gray, W.G. and Schrefler, B.A., 'Thermodynamic approach to effective stress in partially saturated porous media', *Eur. J. Mech. A/Solids* **20** (2001) 521-538.

[22] Mazars, J., 'Application de la mécanique de l'endommagement au comportement non linéaire et la rupture du béton de structure', Thèse de Doctorat d'État, L.M.T., Université de Paris, France, 1984.

[23] Mazars, J., 'Description of the behaviour of composite concretes under complex loadings through continuum damage mechanics', Proc. Tenth U.S. National Congress of Applied Mechanics, J.P. Lamb (ed.), ASME, 1989.

[24] Pijaudier–Cabot, G., 'Non local damage', in H.B. Mühlhaus (ed.), 'Continuum Models for Materials with Microstructure', chapter 4 (Wiley & Sons, Chichester, 1995) 105-143.

[25] Kachanov, M.D., 'Time of rupture process under creep conditions', *Izvestia akademii nauk* **8** (1958) 26-31 (in Russian).

[26] Hassanizadeh, S.M. and Gray, W.G., 'General conservation equations for multi-phase systems: 1. Averaging procedure', *Adv. Water Resources* **2** (1979) 131-144.

[27] Hassanizadeh, S.M. and Gray, W.G., 'General conservation equations for multi-phase systems: 2. Mass, Momenta, energy and entropy equations', *Adv. Water Resources* **2** (1979) 191-203.

[28] Hassanizadeh, S.M. and Gray, W.G., 'General conservation equations for multi-phase systems: 3. Constitutive theory for porous media flow', *Adv. Water Resources* **3** (1980) 25-40.

[29] Lewis, R.W. and Schrefler, B.A., 'The Finite Element Method in the Static and Dynamic Deformation and Consolidation of Porous Media' (Wiley & Sons, Chichester, 1998).

[30] Schrefler, B.A., 'Mechanics and thermodynamics of saturated-unsaturated porous materials and quantitative solutions', *Applied Mechanics Review* **55**(4) (2002) 351-388.

[31] Gawin, D., 'Modelling of Coupled Hygro-Thermal Phenomena in Building Materials and Building Components', Publ. of Łódź Technical University No. 853, Editions of Łódź Technical University, Łódź, 2000 (in Polish).

[32] Pesavento, F., Non-linear modelling of concrete as multiphase porous material in high temperature conditions, Ph.D. thesis, University of Padova, Padova, 2000.

[33] Zienkiewicz, O.C. and Taylor, R.L., 'The Finite Element Method, vol. 1: The Basis' (Butterworth-Heinemann, Oxford, 2000).

[34] Khoury, G.A., Grainger, B.N. and Sullivan, P.J.E., 'Transient thermal strain of concrete: literature review, conditions within specimens and behaviour of individual constituents', *Mag. Concrete Research* **37**(132) (1985) 131-144.

[35] Thelandersson, S., 'Modeling of combined thermal and mechanical action on concrete', *J. Engng Mech, ASCE* **113**(6) (1987) 893-906.

[36] Pearce, C.J., Davie, C.T., Nielsen, C.V. and Bićanić, N., 'A transient creep model for the hygral-thermal-mechanical analysis of concrete', Onate E. & Owen D.R.J. (eds), Proc. Int. Conf. on Computational Plasticity COMPLAS VII (on CD), 1-19, CIMNE, Barcelona, 2003.

[37] Consolazio G.R., McVay M.C. and Rish, J.W., 'Measurement and prediction of pore pressure in cement mortar subjected to elevated temperature', NIST SP 919, Proc. Int. Workshop on Fire Performance of High Strength Concrete, Phan L.T., Carino N.J., Duthin D. and Garboczi E. (eds), NIST, Gaithersburg, MD, February 13-14, 1997, 125-148.

[38] Chaboche, J.L., 'Continuum damage mechanics: Part I – General concepts', *J. Applied Mech.* **55** (1988) 59-64.

[39] Bourgeois, F., Burlion, N. and Shao, J.F., 'Modelling of elstoplastic damage due to desiccation shrinkage', *Int. J. Numer. Anal. Meth. Geomech.* **26** (2002) 759-774.

[40] Coussy, O., 'Mechanics of Porous Continua' (Wiley, Chichester, 1995).